

RESEARCH ARTICLE | JUNE 07 2021

Hydrogen bond effects in multimode nuclear dynamics of acetic acid observed via resonant x-ray scattering

Viktoriia Savchenko; Victor Ekholm ; Iulia Emilia Brumboiu ; Patrick Norman ; Annette Pietzsch ; Alexander Föhlisch ; Jan-Erik Rubensson ; Johan Gråsjö; Olle Björneholm; Conny Sätze ; Minjie Dong; Thorsten Schmitt ; Daniel McNally; Xingye Lu; Pavel Krasnov ; Sergey P. Polyutov ; Faris Gel'mukhanov ; Michael Odelius ; Victor Kimberg  



J. Chem. Phys. 154, 214304 (2021)

<https://doi.org/10.1063/5.0049966>



CrossMark

Articles You May Be Interested In

Nuclear dynamics in resonant inelastic X-ray scattering and X-ray absorption of methanol

J. Chem. Phys. (June 2019)

Multiplexed high resolution soft x-ray RIXS

AIP Conference Proceedings (July 2016)

Soft x-ray RIXS endstation at Sirius

AIP Conference Proceedings (January 2019)

500 kHz or 8.5 GHz?
And all the ranges in between.

Lock-in Amplifiers for your periodic signal measurements



Find out more



Hydrogen bond effects in multimode nuclear dynamics of acetic acid observed via resonant x-ray scattering

Cite as: J. Chem. Phys. 154, 214304 (2021); doi: 10.1063/5.0049966

Submitted: 11 March 2021 • Accepted: 14 May 2021 •

Published Online: 7 June 2021



View Online



Export Citation



CrossMark

Viktoriia Savchenko,^{1,2,3} Victor Ekholm,^{4,5} Iulia Emilia Brumboiu,^{1,6} Patrick Norman,¹ Annette Pietzsch,⁷ Alexander Föhlisch,^{7,8} Jan-Erik Rubensson,⁴ Johan Gråsjö,^{4,9} Olle Björneholm,⁴ Conny Sâthe,⁵ Minjie Dong,⁴ Thorsten Schmitt,¹⁰ Daniel McNally,¹⁰ Xingye Lu,¹⁰ Pavel Krasnov,^{2,3} Sergey P. Polyutov,^{2,3} Faris Gel'mukhanov,^{1,2,3} Michael Odelius,^{11,a)} and Victor Kimberg^{1,2,3,b)}

AFFILIATIONS

¹ Department of Theoretical Chemistry and Biology, KTH Royal Institute of Technology, SE-106 91 Stockholm, Sweden

² International Research Center of Spectroscopy and Quantum Chemistry-IRC SQC, Siberian Federal University, 660041 Krasnoyarsk, Russia

³ Kirensky Institute of Physics, Federal Research Center KSC SB RAS, 660036 Krasnoyarsk, Russia

⁴ Department of Physics and Astronomy, Uppsala University, P.O. Box 516, SE-751 20 Uppsala, Sweden

⁵ MAX IV Laboratory, Lund University, P.O. Box 118, SE-221 00 Lund, Sweden

⁶ Department of Chemistry, Pohang University of Science and Technology (POSTECH), 37673 Pohang, Republic of Korea

⁷ Institute for Methods and Instrumentation in Synchrotron Radiation Research PS-ISRR, Helmholtz-Zentrum Berlin für Materialien und Energie, Albert-Einstein-Strasse 15, Berlin 12489, Germany

⁸ Institut für Physik und Astronomie, Universität Potsdam, Karl-Liebknecht-Strasse 24-25, Potsdam 14476, Germany

⁹ Department of Medicinal Chemistry, Uppsala University, P.O. Box 574, 75123 Uppsala, Sweden

¹⁰ Swiss Light Source, Photon Science Division, Paul Scherrer Institut, CH-5232 Villigen PSI, Switzerland

¹¹ Department of Physics, Stockholm University, AlbaNova University Center, 10691 Stockholm, Sweden

^{a)} Electronic mail: odelius@fysik.su.se

^{b)} Author to whom correspondence should be addressed: kimberg@kth.se

ABSTRACT

A theoretical and experimental study of the gas phase and liquid acetic acid based on resonant inelastic x-ray scattering (RIXS) spectroscopy is presented. We combine and compare different levels of theory for an isolated molecule for a comprehensive analysis, including electronic and vibrational degrees of freedom. The excitation energy scan over the oxygen K-edge absorption reveals nuclear dynamic effects in the core-excited and final electronic states. The theoretical simulations for the monomer and two different forms of the dimer are compared against high-resolution experimental data for pure liquid acetic acid. We show that the theoretical model based on a dimer describes the hydrogen bond formation in the liquid phase well and that this bond formation sufficiently alters the RIXS spectra, allowing us to trace these effects directly from the experiment. Multimode vibrational dynamics is accounted for in our simulations by using a hybrid time-dependent stationary approach for the quantum nuclear wave packet simulations, showing the important role it plays in RIXS.

© 2021 Author(s). All article content, except where otherwise noted, is licensed under a Creative Commons Attribution (CC BY) license (<http://creativecommons.org/licenses/by/4.0/>). <https://doi.org/10.1063/5.0049966>

I. INTRODUCTION

Understanding and modeling quantum nuclear effects in disordered systems, such as liquids, is one of the major challenges of modern condensed matter physics. Hydrogen bonding (HB) responsible for anomalies of liquids and solutions influences numerous important processes in chemistry, biology, and material sciences. Modern x-ray absorption spectroscopy (XAS) and resonant inelastic x-ray scattering (RIXS) are well suited for studies of systems with various types of inter- and intra-molecular interactions.^{1,2} The main advantage of XAS and RIXS is the intrinsic site and element selectivity even in complex systems due to the high localization of core-electrons on a particular atomic center. RIXS further, being a life-time broadening-free spectroscopy, provides ultra-high spectral resolution, thus allowing for the vibrational structure resolution even in the liquid phase.^{3,4} In many molecular systems and at many edges, one of the lowest core-excited states is a dissociative or weakly bound state,^{5,6} into which excitations result in a fast elongation of the molecular bond. In the case of RIXS, this phenomenon (also known as ultrafast dissociation) results in a long vibrational progression and thus brings a unique opportunity to probe the intra- and inter-molecular interactions for large displacements from the equilibrium geometry and to map the potential energy curves (PECs) up to the dissociation limit.^{3,7,8} Since the PEC shape is affected by the local environment of the target molecule, RIXS, due to its spatial sensitivity, becomes a powerful tool to study inter-molecular interactions, local properties, and the structure of disordered systems with controlled magnitude of disorder. Tuning the excitation energy to various core-excited states allows for the localization of the vibrational excitation on a particular bond, thus for the extraction of the PECs along specific bonds, and, particularly, for obtaining more precise information about the HB networks in liquids.

The local structure of pure liquids has been a highly debated topic until now. From a theoretical point of view, we face the fundamental problem of how to describe the nuclear quantum effects in a fluctuating hydrogen-bond network. Due to the high complexity of disordered systems, RIXS of liquids has so far only been simulated with classical molecular dynamics approaches,⁹ which entirely neglects the quantum nuclear dynamics observed experimentally using synchrotron radiation in the latest high-resolution measurements.^{3,10} A step toward understanding the details of the HB network formation in pure liquids was recently made for water^{4,11} and methanol⁶ with the help of high resolution XAS and RIXS experiments and quantum dynamic simulations. Here, we address in detail a more advanced case, acetic acid (ACA), which is one of the simplest carboxyl acids and a very important compound in various biochemical and electrochemical reactions. In a preceding letter by the same authors,¹² it was shown that the effect of the HB formation in ACA provides a very clear fingerprint in the RIXS spectra via the second $O1s^{-1}$ core-excited state, contrary to water and methanol, where the HB results only in more subtle changes in spectra. In the present study, we explore multimode dynamics in ACA under oxygen K-edge excitation and discuss how it varies for the gas and liquid phases. Unlike the water and methanol molecules, ACA has two nonequivalent oxygen atoms at which core-excitations trigger excitations of different vibrational motions. Our analysis is based on accurate *ab initio* and density functional theory (DFT)

calculations of the electronic structure and PECs along several vibrational modes important for the formation of RIXS via both oxygen core-excited atoms. We discuss the results for an isolated ACA molecule (monomer) and an ACA dimer, as the simplest model for the liquid phase. Simulation of the nuclear dynamics in RIXS is performed in the recently proposed mixed time-dependent stationary approach,⁶ when the modes along the dissociative (or quasi-dissociative) PECs are considered by the time-dependent solution of the nuclear Schrödinger equation, while other contributing modes are taken into account by the stationary Franck–Condon approach, allowing for rather cheap simulations as compared to the liquid phase dynamics model.⁴

Super-high resolution, provided by modern RIXS instruments in the liquid phase experiment presented here, makes it possible to obtain vibrationally resolved RIXS and thus to study molecular vibrations triggered by the excitation of core-electrons with unprecedented detail. However, due to the high complexity of the liquid systems, experimental RIXS spectroscopy must be reinforced by theoretical simulations taking into account vibrational dynamics at the quantum level. As a result, our combined theoretical–experimental analysis of RIXS, applied to the study of ACA in gas and liquid phases, allows us not only to obtain new details on the structure and dynamics of the system but also to show, in general, how RIXS spectroscopy can be employed for studying various complex systems.

This paper is organized as follows: We start with the description of the experimental technique in Sec. II A, followed by a discussion of theoretical methods for the electronic structure calculations (Sec. II B) and the mixed time-dependent wave packet and stationary description of the nuclear dynamics in RIXS (Sec. II C). The results and discussions are presented in Sec. III, which begins with a description of normal modes and PEC analysis (Sec. III A). Then, we consider the formation of XAS spectra of gas and liquid ACA (Sec. III B), followed by an analysis of the electronic (Sec. III C) and vibrationally resolved (Secs. III D–III E) RIXS and its excitation energy dependence (Sec. III F) in the isolated ACA molecule and in the ACA dimer. Our findings are summarized in Sec. IV.

II. METHODS

A. Experiment

All measurements were performed at the ADDRESS beamline¹³ at the Swiss Light Source using the SAXES spectrometer¹⁴ at room temperature. We used vertically polarized light with energies at the oxygen K-edge. The resonantly scattered photons were detected at a 90° angle relative to the direction of incoming photon polarization with an experimental resolution of ≈ 45 meV for liquid ACA. A flow cell separating the sample from the vacuum by a 100 nm thick Si_3N_4 window was moved every 5 min to avoid the risk of window rupture under irradiation. The liquid acetic acid from Sigma-Aldrich had a purity level of $\geq 99\%$. The experimental spectra presented here were determined as the sum of the spectra measured at several times (5 min each) for every excitation energy and then normalized by dividing by the number of measurements times the number of detectors. The spectra of all individual scans were shifted to the same energy scale by using a fit to the elastic line before joining them for further data processing. The energy calibration was done using the

O₂ RIXS spectrum.¹⁵ Additional check of the absorption profile was done in our experiment by monitoring the integrated RIXS intensity at various values of the excitation energy across the pre-edge, given general agreement with XAS as shown earlier.¹² For comparison, we reproduce the experimental XAS spectra in Sec. III B taken from the literature for the gas phase¹⁶ and liquid ACA.² In Sec. III C, we also reproduce and discuss the broad range electron photoemission spectra of gas-phase ACA from Ref. 17.

B. Electronic structure theory calculations

In the present study, a number of different methods for the electronic structure theory calculations of the ACA monomer and dimer are used, giving complementary views on the structure and nuclear dynamics of the systems. The equilibrium molecular geometries for the monomer and dimers of ACA were optimized with the MOLCAS quantum chemistry package¹⁸ at the DFT/B3LYP theory level with the ANO-RCC-VTZP basis set.¹⁹ Further calculations of the ground, valence-excited, and core-excited electronic states of an isolated ACA molecule were performed with the restricted active space self-consistent field (RASSCF) method followed by the second order perturbation theory correction (RASPT2) performed in MOLCAS with the same basis set as the DFT calculations. Using of the relativistic ANO-RCC-VTZP basis set invokes scalar relativistic calculations expressed in the Douglas–Kroll Hamiltonian^{20,21} in both the DFT and RASSCF or RASPT2 calculations. The RAS was

configured with eight active electrons and ten active molecular orbitals for the ground state and ten active electrons and 13 active molecular orbitals [including one of the O1s orbitals (at the time) in the RAS1 space] for valence and core-excited states. The choice of active and inactive spaces in RASPT2 was made using an analysis of the ground state molecular orbitals, which are presented in Fig. 1. Shown are the occupied orbital space consisting of 13 orbitals in *a'* symmetry and three orbitals in *a''* symmetry and the eight lowest unoccupied orbitals—six orbitals in symmetry *a'* and two orbitals in symmetry *a''* (Fig. 1).

The RIXS process studied here is triggered by the excitation of a 1s electron from the 1*a'* and 2*a'* orbitals, located on the O_H and O_C oxygen atoms, respectively (see Fig. 2 for the atomic site notation), to an unoccupied orbital, resulting in the formation of the O_H1s⁻¹ and O_C1s⁻¹ core-excited state, respectively. This is in the RIXS process followed by fluorescence decay to the final valence-excited state (a valence electron fills the core-hole vacancy and an x-ray photon is emitted). The transition dipole moments between the ground and core-excited states and core-excited and valence-excited states were computed using the RASSI (Restricted Active Space State Interaction) approach^{22,23} in OpenMolcas.²⁴ Proper treatment of the transition dipole moments is ensured by using the “highly excited state” (HEXS) approach²⁵ within the RASSCF method. The RAS configuration used here describes well the electronic structure of the ground and excited states near the equilibrium geometry, while a much larger active space is needed to properly describe

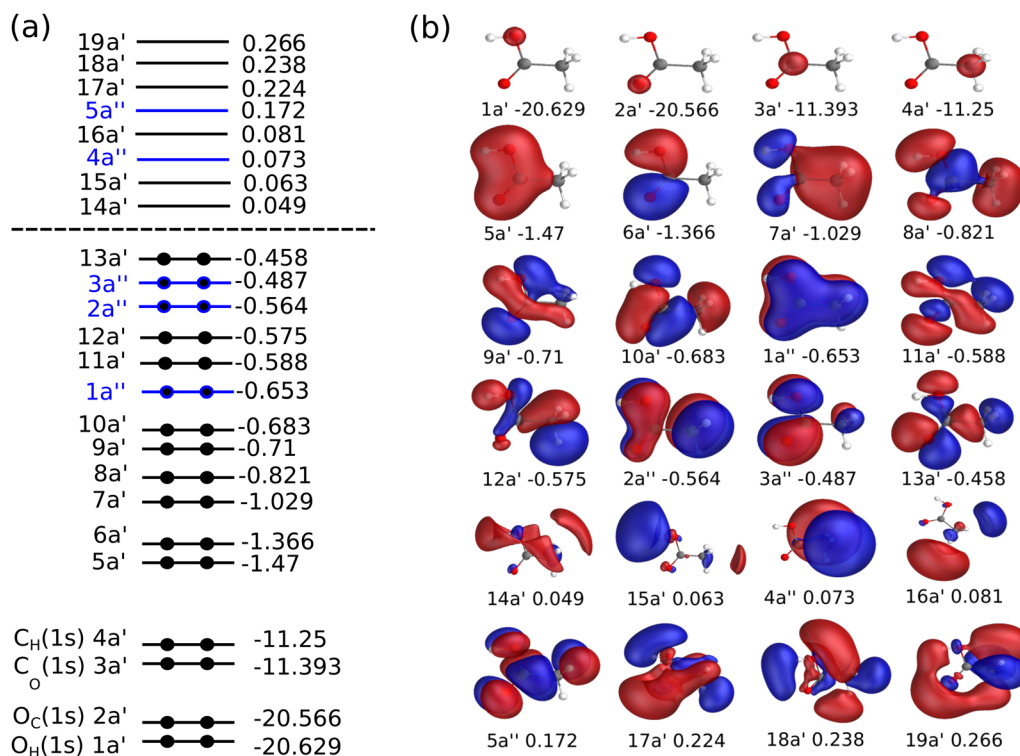


FIG. 1. (a) Schematic picture of the ground state electronic orbitals of the ACA monomer with symmetry constraint. (b) The 24 lowest molecular orbitals computed at the SCF level of theory.

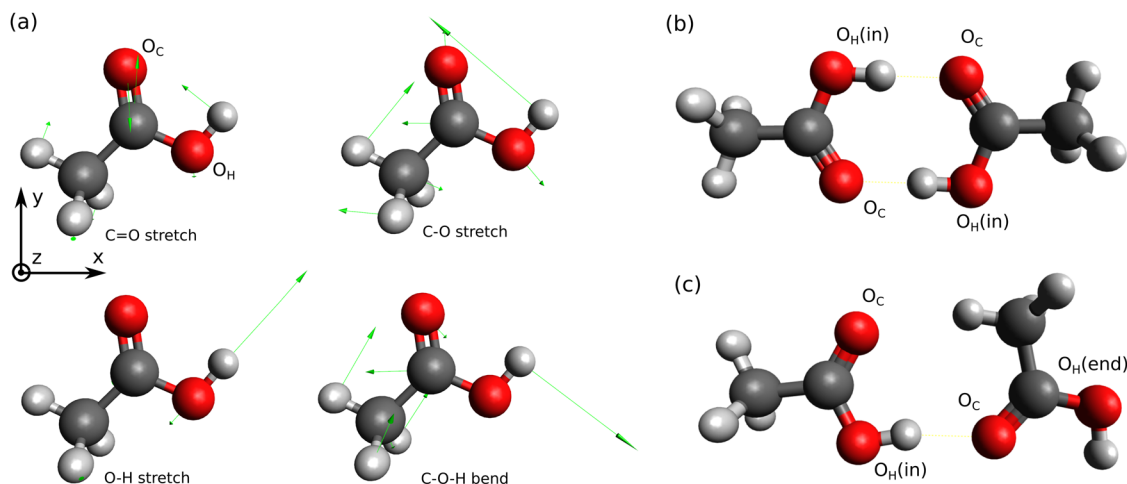


FIG. 2. (a) The four normal modes of ACA that are mainly active at O K-edge excitation are shown. The mode assignment is done following the established assignment from the literature.⁵³ The two non-equivalent cyclic oxygen atoms are labeled O_C and O_H , as referred in the text. The molecular coordinate frame used in the calculations is also shown. Molecular geometries of the cyclic (symmetric) (b) and inverted (c) ACA dimers are shown. The non-equivalent $O_H(\text{in})$ and $O_H(\text{end})$ atoms are labeled.

continuous PECs reaching strongly distorted molecular geometries, since the orbital contributions change sufficiently with the distortion. At a reduced computational cost, we use DFT in the StoBe2014 software for performing scans along the normal modes in order to obtain the PECs (see Sec. III A). For determining the potentials of the ground state and valence-excited and core-excited states of both A' and A'' symmetries, we performed calculations with a gradient corrected Becke88 exchange²⁶ and Perdew86 correlation²⁷ functional. Using the procedure of explicit occupations, we managed to determine A' states from $\sigma \rightarrow \sigma^*$ and $\pi \rightarrow \pi^*$ transitions along with A'' states from $\sigma \rightarrow \pi^*$ and $\pi \rightarrow \sigma^*$ transitions. The TZVP²⁸ basis sets combined with GENA4 auxiliary basis sets were used for all atoms, with exception for the core-excited oxygen, for which we used an IGLO-III basis set²⁹ and an effective core potential for the other oxygen.³⁰ The PECs obtained at the DFT level of theory were shifted accordingly to match the equilibrium geometry energies obtained from RASPT2 calculations. It is worth noting that the PECs computed with the RASPT2 method near the equilibrium geometry well coincide with the corresponding PECs computed with DFT.

For the dimer calculations, the structures of both direct and inverse dimers were optimized with the Gaussian 16 package³¹ using the second-order Møller–Plesset perturbation theory^{32–37} and the cc-pVTZ basis set.^{38–40} The geometry optimization of the dimers also included the counterpoise correction to counter the basis set superposition error.^{41,42} The x-ray absorption spectra near the oxygen K-edge were then computed for the monomer and the regular (cyclic) dimer at the optimized equilibrium geometry of the ground state using the algebraic diagrammatic construction (ADC) level of theory.⁴³ The method is implemented in the Q-Chem 5.1 quantum chemistry software.⁴⁴ For this, we used the core-valence separation (CVS) approximation for the extended second order ADC variant, i.e., CVS-ADC(2)-x^{45–47} and the 6-311++G** basis set.^{48,49} For the monomer, the excitation energies and transition dipole moments from O1s core levels to unoccupied molecular orbitals were computed directly. For the dimer, to reduce the high computational

cost, we replaced the O1s electrons of all O atoms except the core-excited one with effective core potentials (ECPs) of the Stuttgart and Cologne group (ECP2MWB).⁵⁰ The use of ECPs results in an identical spectrum compared to the all-electron calculation, as shown for the π^* region (see Sec. III B 1 and Fig. 6). The total XAS spectrum of the dimer was computed as the sum of individual O atom contributions. In order to make a clear comparison with the experiment, the transitions were broadened using Lorentzian functions of 0.08 eV half width at half maximum (HWHM) and the total spectrum was obtained as a sum over all transitions.

C. Quantum theory of the nuclear dynamics in XAS and RIXS

Due to the nuclear wave packet dynamics in the core-excited states, the electronic XAS spectral peaks are dressed in vibrational progressions. To compute the vibrationally resolved spectra in the present study, we apply the Born–Oppenheimer approximation, decoupling the electronic and nuclear degrees of freedom. The electronic part is obtained by computing the transition dipole moments using *ab initio* methods (Sec. II B). To calculate the nuclear part, we employ the hybrid time-dependent stationary formalism.^{6,7} The vibrationally resolved cross section for the x-ray absorption profile in the time-dependent representation reads⁵¹

$$\sigma_{\text{abs}}(\omega) = \frac{|\mathbf{d}_{\text{cg}}|^2}{3} \int_0^\infty dt e^{i(\omega - \omega_{\text{cg}} + \epsilon_0 + i\Gamma)t} \sigma_{\text{abs}}(t), \quad (1)$$

$$\sigma_{\text{abs}}(t) = \langle \nu_0 | \psi_c(t) \rangle,$$

where ω_{cg} and \mathbf{d}_{cg} are the energy difference and the electronic transition dipole moment between the ground (g) and core-excited (c) states, respectively, ϵ_0 is the zero-point energy of the ground state, and Γ is the lifetime broadening (HWHM) of the core-excited state—in the present case of oxygen K-edge excitation, $\Gamma = 0.08$ eV.⁵² The autocorrelation function $\sigma_{\text{abs}}(t)$ is computed as an overlap

of the ground state vibrational wave function $\langle v_0 |$ and the time-dependent solution of the Schrödinger equation for the core-excited nuclear wave packet $|\psi_c(t)\rangle = e^{-i\hat{h}_c t} |v_0\rangle$ with the nuclear Hamiltonian of the core-excited state \hat{h}_c . Normal coordinates of the ground state are used throughout the paper.

The core-excited states further decay back to the ground electronic (quasi-elastic scattering channel) and valence excited states (inelastic scattering channels) with the emission of another x-ray photon of frequency ω' giving rise to the RIXS cross section, which in the time-dependent representation reads

$$\sigma(\omega', \omega) = \frac{\zeta(\chi, \mathbf{d}_{cg}, \mathbf{d}_{fc})}{\pi} \text{Re} \int_0^\infty e^{i(\omega - \omega' - \omega_{fg} + \epsilon_0 + i\Gamma_f)t} \sigma(t) dt, \quad (2)$$

$$\sigma(t) = \langle \Psi(0) | \Psi(t) \rangle,$$

where the autocorrelation function $\sigma(t)$ is obtained using the integrated core-excited wave packet $|\Psi(0)\rangle$ and the wave packet in the final electronic state $|\Psi(t)\rangle$ is computed as

$$|\Psi(t)\rangle = e^{i\hat{h}_f t} |\Psi(0)\rangle, \quad (3)$$

$$|\Psi(0)\rangle = \int_0^\infty e^{i(\omega - \omega_{fg} + \epsilon_0 + i\Gamma_f)t} |\psi_c(t)\rangle dt,$$

where \hat{h}_f is the nuclear Hamiltonian of the final electronic state, ω_{fg} is the energy difference between the ground and final (f) electronic states, and \mathbf{d}_{fc} is the transition dipole moment on the decay transition between the core-excited and final states. In the present study, we neglect the variation of the transition dipole moment components with the nuclear coordinate and assume it to be a constant value, taken at the equilibrium geometry of the ground electronic state: $\mathbf{d}_{gc} \equiv \mathbf{d}_{cg}(R_0) = \text{const}$ and $\mathbf{d}_{cf} \equiv \mathbf{d}_{fc}(R_0) = \text{const}$. The Frank-Condon approximation is rather good in the present case since the initial wave function $|v_0\rangle$ is localized around the ground state equilibrium geometry, and there is no any sharp variation of the \mathbf{d}_{gc} according to our calculations around the ground state equilibrium geometry. The cross sections (1) and (2) are averaged over random molecular orientations in the gas or liquid phase, giving rise to the pre-factors $d_{cg}^2/3$ and $\zeta(\chi, \mathbf{d}_{cg}, \mathbf{d}_{fc})$ for the XAS and RIXS cross sections, respectively. The details of the orientation averaging and equations for the pre-factors can be found in the [Appendix](#).

The time-dependent approach outlined above allows us to obtain an accurate description of the nuclear dynamics in real time, and it is especially suited for the cases when a strong and fast dynamics is expected, e.g., when a dissociative state is involved. However, this method becomes quite expensive with the increasing number of nuclear degrees of freedom. In order to include several vibrational modes, yet keeping the computational cost relatively low, we used here a mixed time-dependent stationary representation.^{4,6} In this approach, the total nuclear Hamiltonian of the system is written as a sum of time-dependent and time-independent sub-systems,⁶

$$\hat{h}_i = \hat{h}_i^{(m)} + \hat{h}_i^{(n)}, \quad i = g, c, f, \quad (4)$$

neglecting the coupling between the selected subspaces of vibrational modes described in the time-domain (m subspace) and with the stationary Schrödinger equation (n subspace). In the present mixed approximation, the solution of the Schrödinger equation involving the total Hamiltonian \hat{h}_i will take the form of a product of the

time-dependent wave packet $\psi_i^{(m)}(t)$ and stationary eigenfunctions $|v_i\rangle = |v_i^{(1)}, v_i^{(2)}, \dots, v_i^{(n)}\rangle$,

$$|\psi_i^{(m)}(t)\rangle |v_i\rangle, \quad i = c, f. \quad (5)$$

The initial vibrational state in Eqs. (1)–(3) is therefore replaced by

$$|v_0\rangle \rightarrow |\mu_0\rangle |v_0\rangle, \quad \epsilon_0 \rightarrow \epsilon_{\mu_0} + \epsilon_{v_0}, \quad (6)$$

where μ_0 represents zero vibrational level of the time-dependent subspace. Using this, one can formulate the final expressions for the RIXS cross section in the mixed ($mD + nD$) representation used in our simulations,

$$\sigma_{\text{abs}}(\omega) = \text{Re} \sum_{v_c} |\langle v_0 | v_c \rangle|^2 \langle \mu_0 | \Psi_{v_c}(0) \rangle,$$

$$\sigma(\omega', \omega) = \frac{1}{\pi} \text{Re} \sum_{v_f v'_c v_c} \langle v_0 | v'_c \rangle \langle v'_c | v_f \rangle \langle v_f | v_c \rangle \langle v_c | v_0 \rangle$$

$$\times \int_0^\infty e^{i(\omega - \omega' - \omega_{f_0} - \epsilon_{v_f} + \epsilon_{v_0} + \epsilon_{\mu_0} + i\Gamma_f)t} \sigma_{v'_c v_c}(t) dt,$$

$$\sigma_{v'_c v_c}(t) = \langle \Psi_{v'_c}(0) | \Psi_{v_c}(t) \rangle,$$

where $\Psi_{v_c}(0)$ and $\Psi_{v_c}(t)$ are defined as $\Psi(0)$ and $\Psi(t)$, respectively [Eq. (3)], for each stationary vibrational eigenstate v_c in the core-excited electronic state. The complete details of the mixed $mD + nD$ approach can be found elsewhere.⁵ In the present paper, we apply this technique in the $1D + 3D$ form (one time-dependent and three stationary modes) to describe contributions from the four main vibrational modes involved in the spectrum formation (Sec. III A).

III. RESULTS AND DISCUSSION

A. Normal modes analysis and potential energy curves

A theoretical normal modes analysis for the ground electronic state of the monomer and inverted dimer was performed at the B3LYP DFT level of theory, as explained above for the geometry optimization. The acetic acid molecule possesses $3 \times 8 - 6 = 18$ vibrational normal modes, while for the dimer, the number of normal modes becomes $3 \times 16 - 6 = 42$.

1. Monomer

The results of the normal modes analysis for the monomer are summarized in [Table I](#), where the theoretical normal mode frequencies, computed in this work, are compared against the experimental values for the fundamental frequencies known from the literature.⁵³ In the processes studied here, related to the core-excitation of the O K-edge, not all vibrational modes contribute to the XAS and RIXS spectra. To simplify the vibrational analysis, we excluded from our consideration the soft vibrational modes with frequencies $\lesssim 0.1$ eV ($\nu_{10} - \nu_{12}$ and $\nu_{16} - \nu_{18}$), which cannot be resolved in the present RIXS measurements and may only cause a small additional broadening. For the rest of the modes, the core-excited PECs around the equilibrium ($-0.5 \dots 0.5$ a.u.) for all core-excited states were computed and analyzed for vibrational excitation using Huan-Rees parameters, proportional to the displacement of the PECs minima.

TABLE I. Vibrational normal modes types and fundamental frequencies are taken from the literature (Expt.)⁵³ and compared against our normal mode analysis performed with the DFT/B3LYP theory level (Theory) presented in cm^{-1} (eV). The types of the modes are given approximately.

Type	Number	Sym.	Expt., cm^{-1} (eV)	Theory, cm^{-1} (eV)
OH str	ν_1	A'	3583 (0.4442)	3748 (0.4652)
CH ₃ d-str	ν_2	A'	3051 (0.3783)	3162 (0.3925)
CH ₃ s-str	ν_3	A'	2944 (0.3650)	3051 (0.3787)
C=O str	ν_4	A'	1788 (0.2217)	1813 (0.2250)
CH ₃ d-deform	ν_5	A'	1430 (0.1773)	1471 (0.1826)
CH ₃ s-deform	ν_6	A'	1382 (0.1712)	1408 (0.1748)
OH bend	ν_7	A'	1264 (0.1567)	1334 (0.1655)
C–O str	ν_8	A'	1182 (0.1466)	1199 (0.1489)
CH ₃ rock	ν_9	A'	989 (0.1226)	997 (0.1238)
CC str	ν_{10}	A'	847 (0.1050)	857 (0.1064)
OCO deform	ν_{11}	A'	657 (0.0815)	663 (0.0823)
CCO deform	ν_{12}	A'	581 (0.0720)	424 (0.0526)
CH ₃ d-str	ν_{13}	A''	2996 (0.3715)	3110 (0.3861)
CH ₃ d-deform	ν_{14}	A''	1430 (0.1773)	1477 (0.1833)
CH ₃ rock	ν_{15}	A''	1048 (0.1299)	1070 (0.1328)
C=O op-bend	ν_{16}	A''	642 (0.0796)	585 (0.0726)
C–O torsion	ν_{17}	A''	534 (0.0662)	546 (0.0678)
CH ₃ torsion	ν_{18}	A''	93 (0.0115)	42 (0.0052)

Our analysis confirms the quite natural guess that all modes related to the vibration of the CH₃ group are only weakly affected by the core excitation of O atoms, not directly bound to this group, and thus can be neglected in our consideration. The remaining four modes were taken fully into account, as each of them plays an important role at a particular core-excitation. These are the O–H (ν_1), C=O double bond (ν_4), and C–O single bond (ν_8) stretching modes, alongside the C–O–H bending (ν_7) mode. The nuclear motion related to these four normal modes is illustrated schematically in Fig. 2(a) along with the molecular frame coordinate system used in our calculations. Two modes—C–O–H bend and C–O stretch—have rather close vibrational quanta and thus are coupled to each other. This fact also follows from the atomic motion pattern for the two modes, shown in Fig. 2(a).

As mentioned above, the PECs along these four chosen normal modes were computed at the DFT theory level using the StoBe2014 software and shifted using more accurate RASPT2 energy calculations at the equilibrium geometry. In the present study, we focus on RIXS via the two lowest core-excited state at the O_C and O_H K-edge, i.e., excitation of 1σ and 2σ electrons, respectively, to the two lowest unoccupied orbitals of a' and a'' symmetries, commonly abbreviated as π^* and σ^* core-excited states. For the valence excited state—final states of resonant inelastic scattering channels, we limit our detailed exploration of the PECs to four electronic states, lowest in energy for each type of symmetry excitation: $\sigma-\pi^*$, $\sigma-\sigma^*$, $\pi-\sigma^*$, and $\pi-\pi^*$. PECs of the ground, core- and valence-excited states along the four normal modes considered in our simulations are summarized in Fig. 3.

Analysis of the PECs according to the Franck–Condon principle allows us to predict roughly the modes with the largest contribution to the vibrational excitation. Indeed, when the PECs of the ground and core-excited states are parallel, only the lowest

vibrational level is excited, resulting in no vibrational progression in the spectra. From this point of view, one can see that the C=O stretching mode contributes largely to the transition to the first core excited state at the O_C K-edge; the first O_H $1s \rightarrow \pi^*$ core-excited state results mainly from C–O–H bend and C–O stretch modes, whereas the second O_H $1s \rightarrow \sigma^*$ state is dissociative along the O–H bond, and due to this, the O–H stretching mode is the one largely involved in this excitation channel. This simplified multimode analysis can be applied as a basis for mode selection to be further used in accurate simulations based on the wave packet technique. Detailed analysis of the vibrationally resolved XAS and RIXS spectra based on the wave packet simulations is given below in Sec. II B.

2. Inverted dimer

For the case of the ACA dimer, the accurate normal mode analysis becomes much more complex due to the large number of normal modes and their quasi degeneracy. Two isomers of the ACA dimer considered in this study are shown in Fig. 2—the symmetric dimer (b) and the inverted dimer (c). In this section, we will focus on the mode analysis performed for the inverted dimer. The main reason for this choice is that a perfectly symmetric dimer is not found in the real liquid due to fluctuating surroundings and large abundance of molecular chains. Moreover, due to symmetry, the doubly degenerated vibrational modes of a fully symmetric cyclic dimer become strongly coupled and indistinguishable in the analysis. For consistence with the calculations of the monomer where four normal modes were identified as important, we focus on the corresponding four modes of the dimer. The four main modes discussed in the case of the monomer are quasi-degenerated in the dimer, given that there are two quasi-equivalent sites. These eight vibrational modes are collected in Table II, in analogy to the vibrational modes of

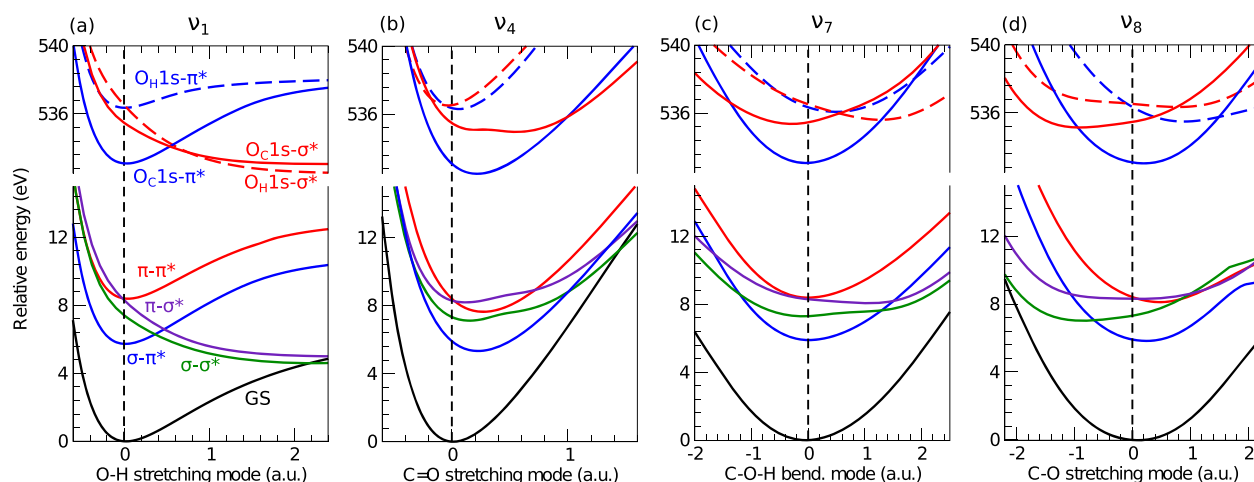


FIG. 3. Potential energy curves for the ground and lower valence- and core-excited states of monomer in normal coordinates of the O–H stretch (a), C=O stretch (b), C–O–H bend (c), and C–O stretch (d) modes (ν_1 , ν_4 , ν_7 , and ν_8 , respectively; see Table I). The state assignment is shown in plot (a). The PEC shapes in a broad range are computed using the DFT method, while the vertical excitation energies are taken from accurate RASPT2 calculations (see the text for more details).

the monomer. To avoid confusion, the normal modes of the dimer are denoted by a superscript d as in ν_i^d .

Similar to the monomer, a limited number of modes give sufficient contribution to the spectra relating to a particular core level. Here, we choose four relevant vibrational modes with strong vibrational contributions when excited at the O_C (ν_9^d , ν_{10}^d) and O_H (in) edges; their potential energy curves are presented in Fig. 4. Let us note the presence of the two non-equivalent O_H atoms in the inverted dimer: O_H (in)—participating in the formation of the HB—and O_H (end)—not participating in the HB formation. The O_H (end) group excitation is rather similar to the one discussed for the monomer and thus omitted here.

Potentials for the dimer are computed at the DFT level of theory (see Sec. II B) and are shifted according to the ADC(2)-x calculations for the excitation energies at the equilibrium geometry. For the O–H stretching mode [Fig. 4(a)], the two lowest $O_H 1s - \pi^*$ core-excited states are very weakly coupled (adiabatic curves show a crossing at 0.35 a.u.); the lowest π^* state (thick blue solid line) shows a much

stronger transition cross section compared to the second π^* state (thin blue solid line), making the diabatic representation acceptable in this case. The single state DFT calculations, however, fail to describe properly the core-excited PEC (gray line).

For comparison, potentials along the corresponding vibrational modes of the monomer are shown in Fig. 4 with dashed lines. Comparison between the core-excited PECs of the monomer and dimer shows sufficient differences, altering the nuclear wave packet dynamics and, as a result, the XAS and RIXS spectra as discussed in Secs. III B–III F. The key difference in the PECs of the monomer and the dimer can be observed with elongation of the O–H stretching mode, which is strongly affected by the HB formation. Indeed, the formation of a second PEC minimum in the ground and core-excited states is observed, corresponding to a proton transfer configuration. This effect is also evidenced from the change in the molecular orbital shape of the $O_H 1s - \pi^*$ core-excited state at three different positions of the H atom, shown in Fig. 5. One can see that the electronic density distributions at equilibrium geometry ($q = 0.0$) and near the second minimum ($q = 1.5$ a.u.) are mirrored.

TABLE II. Selected vibrational normal modes of the inverted dimer found from the analysis at the DFT/B3LYP theory level; analog of monomer's vibrational motion is given in the left column.

Monomer analog	Number	Theory, cm^{-1} (eV)
OH str (end)	ν_1^d	3743 (0.4641)
OH str (in)	ν_2^d	3433 (0.4257)
C=O str (in & end)	ν_9^d	1789 (0.2218)
C=O str (in & end)	ν_{10}^d	1763 (0.2186)
OH bend (in)	ν_{15}^d	1426 (0.1768)
OH bend (end)	ν_{16}^d	1418 (0.1758)
C–O str (in)	ν_{19}^d	1262 (0.1564)
C–O str (end)	ν_{20}^d	1219 (0.1512)

B. X-ray absorption spectra: Gas vs liquid phase

1. Change in the electronic XAS with HB formation

Theoretical XAS spectra computed at the ADC(2)-x theory level are shown in Fig. 6 for the isolated acetic acid and the molecular dimer, in comparison to gas phase and liquid experiments from the literature.^{2,16} In the liquid ACA, as discussed in detail recently,¹² the symmetric dimer gives a minor contribution, while short molecular chains with non-bonded “end” OH groups can be found in abundance. However, for the sake of better understanding, let us focus here on the two distinct cases of ACA: monomer, as a clear representative of the gas phase, and symmetric dimer, as a representative of the case when OH groups are fully involved in the HB formation. Indeed, the comparison of monomer against symmetric dimer simulations allows us to clearly see the HB effect. In

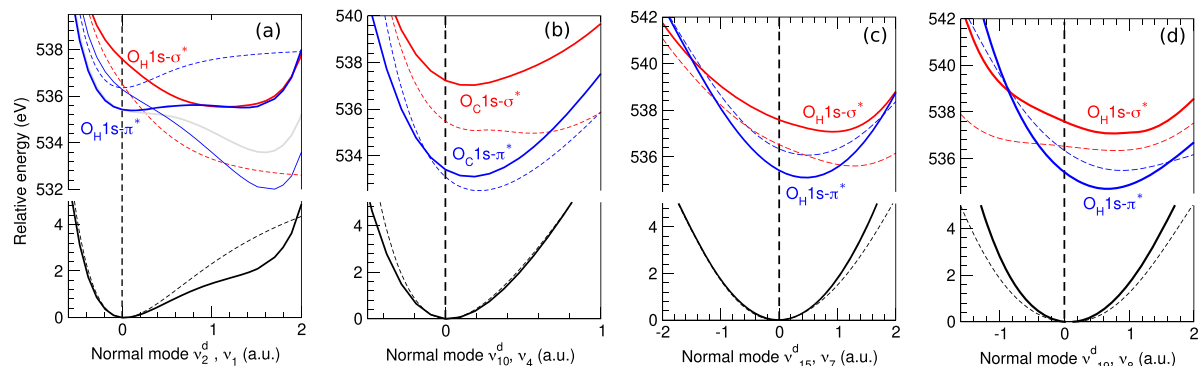


FIG. 4. Comparison of the PECs for the monomer (dashed curves) and inverted dimer (solid curves). The ground state (black) and core-excited states of π (blue) and σ (red) symmetries are shown along the four main modes, similar to the main normal modes discussed for the monomer: (a) $O_H 1s^{-1}$ along the O–H stretching mode (v_2^d, v_1); (b) $O_C 1s^{-1}$ along the O=C stretching mode (v_{10}^d, v_4); (c) $O_H 1s^{-1}$ along v_{15}^d, v_7 ; and (d) $O_H 1s^{-1}$ along v_{19}^d, v_8 . The thin blue curve in panel (a) shows a weak π -state, having non-adiabatic coupling with the lowest strong π -state, and the gray line represents the single state DFT simulation of the lowest $O_H 1s \rightarrow \pi^*$ state (see the text).

the theoretical analysis of Fig. 6, only electronic transitions are taken into account, neglecting the vibrational structure, and the spectral profiles are computed as a sum of transition intensities convoluted with Gaussian functions of width $\Gamma = 0.08$ eV, modeling the lifetime broadening on core-excitation.

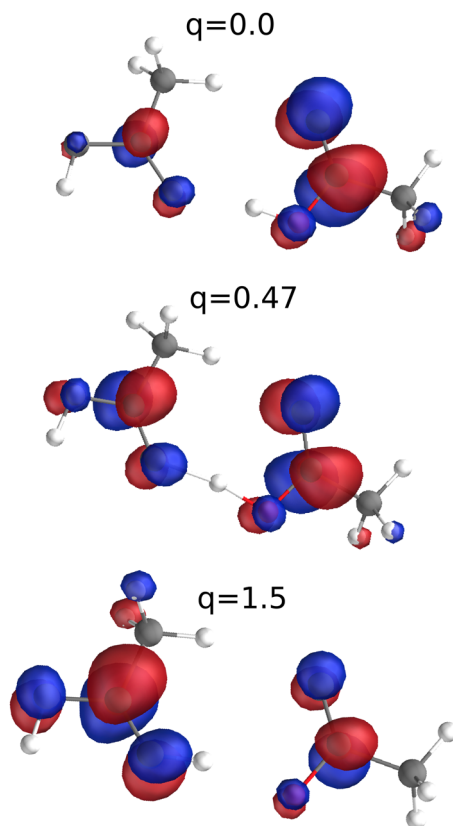


FIG. 5. Modification of the $O_H 1s \rightarrow \pi^*$ core-excited state molecular orbitals with the elongation of the O–H bond at the HB, showing a proton transfer in the inverted dimer.

The lowest energy XAS feature at around 532 eV for both monomer (532.0 eV) and dimer (532.1 eV) shows a well separated peak, corresponding to the excitation of the $1s$ -electron of the O_C atom to the lowest unoccupied molecular orbital, and can be assigned mainly as a $2a' \rightarrow 5a''$ transition. It is worthwhile to note that the order of the ground state virtual orbital space shown in Fig. 1 experiences sufficient relaxation and reorganization so that the $2a'^{-1} 5a''^{11}$ core-hole state becomes the lowest in the π (a'') symmetry. The formation of the hydrogen bond in the dimer results in a shift of this peak to higher energy by 0.3 eV.

The second feature of the XAS near 535 eV has a much more complex structure. In the case of the monomer, this peak's maximum is located at 535.0 eV and is formed mainly by the two lowest core-excited states on the O_H site ($O_H 1s \rightarrow \sigma^*$ and $O_H 1s \rightarrow \pi^*$) with a small contribution from the $O_C 1s \rightarrow \sigma^*$ excitation; in the molecular orbital picture, these core-excited states can be assigned to $1a'^{-1} 15a'^1$, $1a'^{-1} 5a''^{11}$, and $2a'^{-1} 15a'^1$, respectively (see Fig. 1). In the case of the dimer, when the two HBs are formed, the peak's maximum is 534.6 eV and its nature changes drastically. It is formed exclusively by the contribution from the $1a' \rightarrow \pi^*$ transition, lowered in energy by 0.9 eV as compared to the monomer case according to the ADC(2)-x simulations. The $1a' \rightarrow \sigma^*$ excitation is shifted to a much higher energy range and its intensity is significantly reduced.² As mentioned before, in the real liquid ACA, the picture can be described by a combination of two limiting cases discussed here: no-HB (monomer) and full-HB (symmetric dimer). The experimental XAS, reproduced in Fig. 6, shows only a small spectral shift of the O_H peak, leaving hidden all the dramatic changes in the electronic structure caused by the formation of the HBs in the liquid. It is worth noting that the XAS of the inverted dimer¹² resembles an overlap of the top and bottom panels of Fig. 6 and also gives quite good agreement with the experimental profile of the liquid ACA. Obviously, the HB effect is not possible to uncover with XAS measurements, while RIXS measurements contain a distinct signature of the HB formation (Sec. III D 2).

2. Vibrational structure of the XAS profile

In the present paper, we focus our study of RIXS to the two lowest spectral features in XAS: (1) near 532 eV, corresponding to

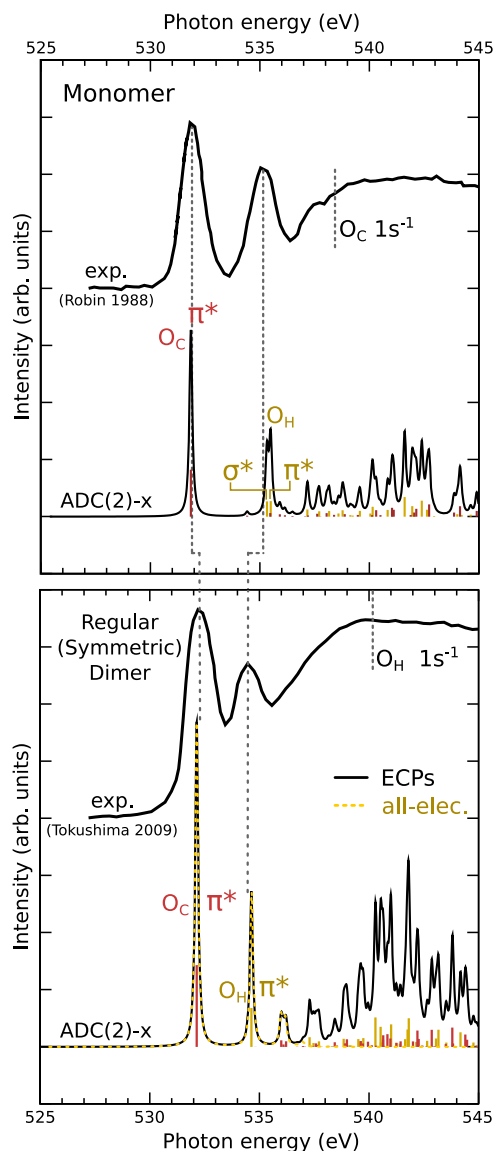


FIG. 6. Theoretical O K-edge XAS for the isolated acetic acid (top panel) and symmetric molecular dimer (bottom panel) compared with experimental gas phase¹⁶ and liquid² spectra. The excitation of the 1s electrons of O_C (red bars) and O_H (yellow bars) is shown. The 1s photoionization energies for O_C and O_H, 538.29 eV and 540.09 eV, respectively,⁵⁴ are marked by the dotted lines. The theoretical spectra are shifted by 0.44 eV toward higher photon energies to align the calculated monomer π^* peak to the π^* peak of the experimental gas phase spectrum. The calculated spectra have been convoluted with Lorentzian functions with HWHM = 0.08 eV, accounting for the lifetime broadening; nuclear dynamics is not taken into account. The dimer XAS spectrum obtained with the ECP approach (bottom panel, black line) is identical to the XAS spectrum computed including all O1s electrons (bottom panel, yellow dotted line).

the core-excitation of the O1s orbital located at O=C group (O_C1s \rightarrow π^*), and (2) near 535 eV, contributed from the core-excitation of the O1s orbital of the OH group (O_H1s \rightarrow σ^* and O_H \rightarrow π^*). According to our *ab initio* simulations at both ADC(2)-x and

RASPT2 levels, the intensity of the O_C1s \rightarrow σ^* transition is much smaller as compared to other excitation intensities, and thus, we neglect this transition in our analysis. The character of the PECs and vibrational excitations in these three core-excited states define strongly the formation of the vibrational profiles. The vibrational contributions to the XAS for the isolated ACA molecule are presented in Fig. 7, where the theoretical XAS profile was calculated taking into account the contribution from four vibrational modes $\nu_1, \nu_4, \nu_7, \nu_8$, using a mixed representation 1D (time-dependent) + 3D (stationary) [see Eq. (7)]. The XAS calculations of Fig. 7 were done using the PECs presented in Fig. 3. The transition energies and transition dipole moments were computed at the RASPT2 theory level (Sec. II B), in excellent agreement with the ADC(2)-x XAS calculations discussed above.

The vibrational contribution to the first peak, related to O_C1s \rightarrow π^* excitation, comes mainly from the C=O stretching mode (ν_4), which shows a broad vibrational progression causing the broadening of the XAS resonance (see the red curve in Fig. 7). The core-excited PECs of the other modes are nearly parallel to the ground state PECs (Fig. 3), resulting in no vibrational excitations in XAS. The second resonance feature, centered at 535.0 eV, is formed by contributions from the O_H1s excitation to the π^* and σ^* states in the gas phase (monomer). The O_H1s \rightarrow σ^* state is strongly dissociative [see Fig. 3(a)] along the O–H bond (ν_1 stretching mode), resulting in a broad XAS resonance, masking small vibrational progressions from the other (bound) modes. The dissociative character of this state induces a fast propagation of the core-excited nuclear wave packet toward the O–H bond elongation, which results in a strong vibrational progression in the RIXS of gas phase molecules (Sec. III D 2). In the liquid phase, however, the O_H1s \rightarrow σ^* state does not contribute to the second resonant feature in XAS, as explained above, and only the O_H1s \rightarrow π^* state forms this peak.

According to the PECs for the O_H1s \rightarrow π^* core-excited state, the O–H stretching mode (ν_1), being the most important in the case of the O_H1s \rightarrow σ^* state, gives no vibrational excitation in the present case, since the PECs of the ground and core-excited states are

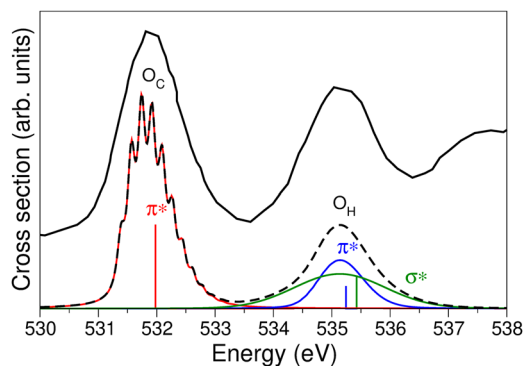


FIG. 7. Theoretical vibrational XAS spectra of the monomer for O_C1s \rightarrow π^* excitation (red curve) and O_H1s \rightarrow π^* and 1s \rightarrow σ^* excitations (blue and green curves, respectively): the total calculated XAS is shown with the black dashed line. Vibrational contribution from the four most active normal modes ν_1, ν_4, ν_7 , and ν_8 (Table I) is taken into account. The electronic excitation energies are shown by the sticks of corresponding color. The theoretical XAS spectrum is shifted by -1.1 eV for comparison with the experiment (black solid line) for the gas phase ACA.¹⁶

parallel. The following question arises: Why does the core-excitation to the π^* state located on the C=O bond result in a strong vibrational excitation ($O_C 1s \rightarrow \pi^*$ resonance), while the $O_H 1s$ excitation located around the O–H bond results in no change in the bond-length? The reason for this is as follows: The linear combination of the atomic orbitals (LCAO) forming the $O_C 1s \rightarrow \pi^*$ states includes contributions from π -orbitals located on both the O and C atoms, which results in a strong modification of the O–H bond length under core-excitation. However, in the case of the $O_H 1s \rightarrow \pi^*$ excitation, the π -orbital has no contribution from the H atom, resulting in no change in the O–H bond length equilibrium compared to the ground state. The vibrational broadening of $O_H 1s \rightarrow \pi^*$, obviously noticeable in the theoretical curve of Fig. 7, appears due to the strong contribution from the C–O–H bending (ν_7) and C–O stretching (ν_8) normal modes. The core-excited π^* state includes contributions from π -orbitals located on O_H and neighboring C atoms, resulting in a sufficient change in the equilibrium O–C distance and C–O–H angle under core-excitation [see Figs. 3(c) and 3(d)].

The calculated vibrational XAS spectrum is in good agreement with the experimental one, shown by the black solid line in Fig. 7. Taking into account the vibrational contribution leads not only to spectral broadening, but can also shift the top resonance energies, as observed, for example, in the case of the $O_H 1s \rightarrow \pi^*$ excitation: compare the electronic transition (blue stick) and the top of the vibration profile (blue line) in Fig. 7.

The presented vibrational analysis is done for the case of the gas phase molecule; nonetheless, it allows us to explain qualitatively the vibrational XAS for the liquid phase as well. Indeed, the HB formation results in the shift to higher energies and decrease in intensity of the $O_H 1s \rightarrow \sigma^*$ excitation, but it has no effect on the PECs of the $O_H 1s \rightarrow \pi^*$ excitation.¹² As evident from the PECs for the inverted dimer (see Fig. 4), the $O_H 1s \rightarrow \pi^*$ PEC of the dimer is also bound with an equilibrium distance lying near the ground state geometry, resulting in no excitation of the O–H stretching mode. The vibrational broadening of the XAS peak comes—in very close analogy to the monomer—from the excitation of the two other vibrational modes, ν_{15}^d and ν_{19}^d , where the core-excited PECs are similar to the corresponding ν_7 and ν_8 modes of the monomer. The vibrationally resolved calculations can be done by taking into account solely the $O_H 1s \rightarrow \pi^*$ core-excited state for the formation of the second peak at 535 eV, in quite reasonable agreement with the liquid phase experimental XAS (Fig. 6). The change in the core-excited $O_C 1s \rightarrow \pi^*$ PEC for the C=O stretching mode is also rather small due to HB formation [see Fig. 4(b)], yielding a vibrational XAS profile for the peak at 532 eV that is very similar to the one obtained for the gas phase.

C. RIXS via the lowest $O_C 1s$ and $O_H 1s$ core-excited states

In this section and in Secs. III D–III F, we present a detailed analysis of the RIXS spectra and discuss the dynamical aspects using the energy detuning from the top of the resonances. We also make a comparison of the formation of the gas phase and liquid phase RIXS spectra. Let us start with a discussion of the electronic RIXS spectra, neglecting for a while the vibrational dynamics. Figure 8 shows the electronic RIXS for excitations at 532 eV— $O_C 1s^{-1}\pi^*$ state

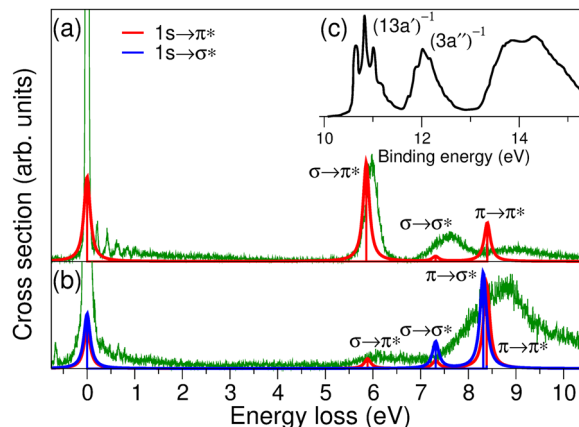


FIG. 8. Theoretical (monomer) and experimental (liquid) RIXS spectra neglecting the vibrational dynamics for the scattering via the first $O_C 1s^{-1}$ (a) and second $O_H 1s^{-1}$ (b) XAS features (see Fig. 6). The theoretical spectra are computed at the RASPT2 theory level for the isolated ACA molecule; red and blue lines correspond to the RIXS channel via the $1s \rightarrow \pi^*$ and $1s \rightarrow \sigma^*$ core-excited states, respectively. The corresponding experimental spectra obtained in this work (green lines), as well as photo-emission spectra [panel (c)],⁵⁴ are shown for comparison. The experimental RIXS spectra are normalized to fit the maximum intensity of the theoretical inelastic band. An energy loss scale is used: $E_l = \omega - \omega'$. The peak at ± 0.66 eV seen in this and all other experimental spectra is a spectrometer artifact and should be neglected.

[Fig. 8(a)]—and at 535 eV— $O_H 1s^{-1}\pi^*, \sigma^*$ [Fig. 8(b)]. Theoretical spectra, computed for an isolated ACA molecule, are compared with experimental measurements in the liquid phase (green lines) and the photoelectron spectrum⁵⁴ [Fig. 8(c)]. The intensity of the electronic transitions is shown with the vertical lines according to the values of the transition dipole moments collected in Table III, while the theoretical spectra are obtained by a Lorentzian convolution with the width of 0.08 eV to simulate the experimental and vibrational

TABLE III. Components of the transition dipole moments ($\times 10^{-2}$ a.u.) in the molecular frame (see Fig. 2) for all studied RIXS channels and the coefficient $\zeta_{cf}(\chi)$ ($\times 10^{-8}$ a.u.) for the measurement angle $\chi = 90^\circ$.

Core-excited	Final state	d_x	d_y	d_z	$\zeta_{cf}(90^\circ)$
$O_C 1s \rightarrow \pi^*$	GS	0	4.87	0	75.1
	$\sigma - \pi^*$	-6.06	0	-0.26	87.3
	$\sigma - \sigma^*$	0	1.16	0	4.26
	$\pi - \sigma^*$	0.13	0	0.01	0.04
	$\pi - \pi^*$	0	-3.28	0	34.0
$O_H 1s \rightarrow \pi^*$	GS	0	-2.53	0	5.47
	$\sigma - \pi^*$	-0.11	0	-1.46	1.38
	$\sigma - \sigma^*$	0	1.12	0	1.08
	$\pi - \sigma^*$	0.17	0	-0.04	0.02
	$\pi - \pi^*$	0	-3.73	0	11.9
$O_H 1s \rightarrow \sigma^*$	GS	2.82	0	1.00	10.7
	$\sigma - \pi^*$	0	0.10	0	0.01
	$\sigma - \sigma^*$	-1.30	0	2.00	5.19
	$\pi - \sigma^*$	0	4.54	0	18.5
	$\pi - \pi^*$	-0.70	0	0.15	0.58

broadening. For the RIXS spectra, an energy loss scale defined as $E_l = \omega - \omega'$ is used throughout the paper.

The low energy loss region of the spectra in Fig. 8 ($E_l \leq 5$ eV) corresponds to the so-called quasi-elastic RIXS channel. This channel is electronically elastic, leading back to the ground state (i.e., the final state is the electronic ground state), yet it is inelastic in terms of the vibrational excitations through the induced nuclear dynamics in the core-excited state. As we have shown before for several systems,^{4,6–8} the vibrational resolution of the quasi-elastic RIXS channel can provide important information about the PECs, the molecular structure, and the formation of the HB. We will discuss this method applied to ACA in Sec. III D 2 together with the full consideration of the multimode nuclear dynamics.

Above 5 eV energy loss, the theoretical RIXS spectrum consists of a number of peaks, related to inelastic scattering channels to a number of valence-excited final states. In the present paper, we singled out only a few contributions to RIXS, namely, from the states where PECs can be calculated accurately (see Fig. 3). The set of four states, abbreviated $\sigma - \pi^*$, $\sigma - \sigma^*$, $\pi - \sigma^*$, and $\pi - \pi^*$, is lowest in each electronic configuration symmetry, which makes it more easy to distinguish an isolated PEC in our simulation (Sec. II B). Red lines describe the RIXS via π^* core-excited states with $O_C 1s$ (a) and $O_H 1s$ (b) core-holes. In this case, the contribution from the final valence state with an electron in π^* is dominating, while the contribution from the final σ^* states is suppressed, as they can only be reached by a dipole forbidden two electron transition. The RIXS via the $O_H 1s \rightarrow \sigma^*$ state (blue line), on the contrary, is formed by the contribution from valence states with a one-electron excitation to a σ^* orbital, while π^* two-electron excitations are suppressed. The comparison of theory against experimental RIXS spectra (green lines), measured in the liquid phase, gives rather good qualitative agreement.

It is also useful to discuss the RIXS profile in connection with the electron photoemission spectrum (PES),⁵⁴ shown for comparison in Fig. 8(c). The first peak in the RIXS spectrum near 6 eV energy loss is assigned to an excitation of an electron from the highest occupied molecular orbital (HOMO) $13a'$ to the lowest unoccupied molecular orbital (LUMO) $5a''$. This corresponds to the peak at the lowest binding energy in PES with ionization from $13a'$. The second strong feature of PES arises from the ionization of a HOMO-1, a $3a''$. In the case of RIXS, it corresponds to the excitation of HOMO-1 to LUMO, $3a''^{-1}5a''^1$, assigned as the $\pi - \pi^*$ features near 8 eV and 9 eV of the experimental RIXS in the plot (a) and (b), respectively (see Fig. 8). The energy difference in the case of $O_C 1s$ (a) and $O_H 1s$ (b) excitation can be explained particularly by the vibrational effects (see Sec. III E). The broad low intensity feature in the higher energy loss range in RIXS is assigned to numerous highly excited valence states not considered in the present study. This corresponds to the third broad peak covering the range of 13–15 eV binding energy in PES, which results from overlap of the photoionization from several orbitals ($3a''$, $12a'$, and $11a'$).^{17,54,55}

The small disagreement between theoretical electronic and experimental RIXS can be explained and has several reasons (sources of errors): (i) difference in gas phase and liquid phase energies due to solvation effects, not taken into account at the present level of theory; (ii) inaccuracies in the calculation of transition energies; and (iii) vibrational dynamics effect (see the more detailed discussion

in Sec. III D 2). Indeed, the PECs of the valence excited states are expected to be much more affected by the HB effects as compared to the ground state, showing only minor differences (see Fig. 4). These differences in the shape and energy position of the PEC of the monomer and dimer could be responsible for the occasional disagreements between simulation and experiment in both electronic energy and vibrational structure. However, simulations of PECs for the valence-excited states for the dimer, performed at the same theory level as for monomer, become very expensive and thus were omitted in the present study. It is important to note that for comparison with the experiment, the $1s - \sigma^*$ channel (blue line) has to be excluded, since it is not present in the core-excitation of the liquid phase,¹² as discussed already (see Sec. II A).

D. Quasi-elastic RIXS channels: Multimode vibrational dynamics

The quasi-elastic scattering channel in RIXS, when the molecule decays back to the ground electronic state, becomes a well-established tool to study ultra-fast core-excited nuclear dynamics^{4,6,7} and to map the ground state potential energy surface in a broad energy range^{3,5,56,57} for both gas and liquid phase targets. Indeed, in many molecules, the low-lying core-excited states have antibonding character, leading to a fast dissociation of a light hydrogen atom even during the ultra-short core-hole lifetime. This results in a spread of the core-excited vibrational wave packet in a broad range of the nuclear coordinate, which, in turn, gives rise to a long vibrational progression in RIXS, allowing for fine mapping of the potential energy curves. This phenomenon is also clearly observed for the OH bonds in an isolated ACA molecule. However, contrary to many other liquids (e.g., water,^{4,11} methanol,⁶ and acetone⁵⁷), we found a dramatic dependence of this effect on the HB formation in the liquid phase. In Secs. III D 1 and III D 2, we discuss the quasi-elastic RIXS spectra at the $O_C 1s$ and $O_H 1s$ excitations in ACA and compare it with the experimental RIXS spectrum for the liquid phase. It is worth noting that the large intensity of the experimental elastic line at $E_l = 0$ is due to the contribution from Thomson scattering, which is ignored in our theory.

1. RIXS via the $O_C 1s \rightarrow \pi^*$ resonance

The analysis of the excitation of the individual vibrational modes in the quasi-elastic RIXS channel via the O_C resonance along with the experimental spectrum is shown in Fig. 9(a). The $O=C$ stretching mode gives the main contribution to the vibrational progression in RIXS with a small contribution from the ν_8 mode in agreement with experiment. The core-excited state PEC minima along two other considered modes coincide with the ground state PEC minimum, resulting in zero excitation for these modes. Indeed, the XAS and RIXS calculations obtained by taking into account three modes (ν_1 , ν_4 , and ν_7) are almost indistinguishable from the spectra obtained using only the $C=O$ stretching mode ν_4 .

Theoretical multimode RIXS spectra are in good agreement with the liquid phase experiment. The small deviation in vibrational frequency is explained by the changes in the ground state PEC in the liquid phase. Indeed, the ground state PEC along the $C=O$ stretch computed for the dimer is more shallow compared with the monomer [see the black solid lines and black dashed lines in Fig. 4(b)], resulting in a smaller vibrational quantum in the liquid

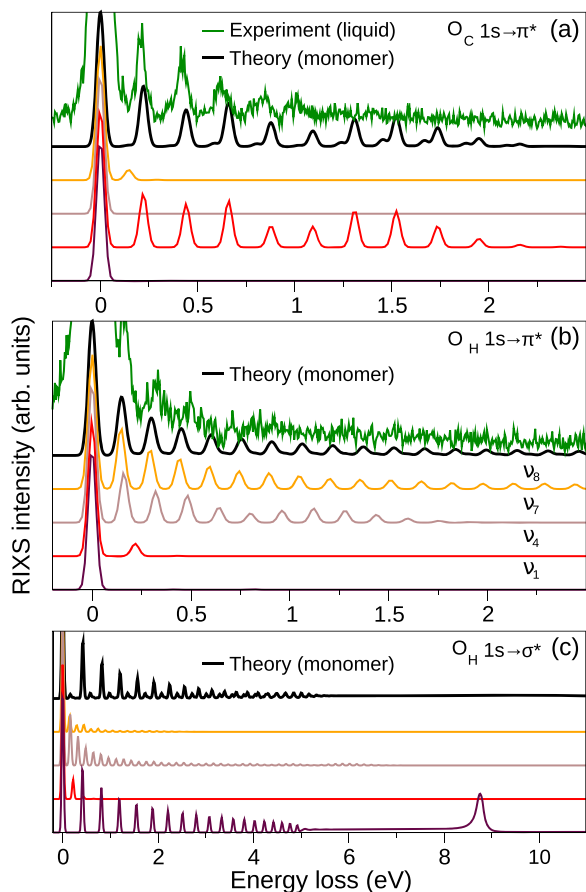


FIG. 9. Multimode theoretical RIXS from gas phase ACA (thick black line) via $O_C 1s \rightarrow \pi^*$ (a), $O_H 1s \rightarrow \pi^*$ (b), and $O_H 1s \rightarrow \sigma^*$ (c) core excited states. The excitation energy is tuned to the top of the absorption peaks at 532 eV (a) and 535 eV [(b) and (c)]. Individual contributions from the four main modes ν_1 , ν_4 , ν_7 , and ν_8 (see Table I) are shown [labeled in the panel (b)]. Experimental RIXS from liquid ACA (green line) is shown in the plots (a) and (c) for comparison.

phase. This trend is in agreement with IR and Raman spectroscopy studies.^{58,59} The dependence of the detuning for the quasi-elastic RIXS channel via the O_C resonance for theory and experiment is discussed later (Fig. 12).

2. O_H resonance: Contribution from $1s \rightarrow \pi^*$ and $1s \rightarrow \sigma^*$ states in gas and liquid ACA

Let us now consider the quasi-elastic part of the RIXS spectra via the $O_H 1s$ resonances. The situation is here significantly different from the case of $O_C 1s$ excitation due to the presence of the two close-lying $1s \rightarrow \pi^*$ and $1s \rightarrow \sigma^*$ core-excited states (Figs. 6 and 7). These two states have qualitatively different character, one being a bound state ($O_H 1s \rightarrow \pi^*$) and the other being a dissociative state ($O_H 1s \rightarrow \sigma^*$) (Fig. 3), resulting in qualitatively different RIXS profiles shown in Figs. 9(b) and 9(c), respectively. The $O_H 1s \rightarrow \sigma^*$ core-excited state in isolated ACA is strongly antibonding resulting in a fast propagation of the core-excited wave packet toward elongation of the O–H bond (ν_1 normal mode). This

dynamics is clearly reflected in the RIXS profile for the ν_1 mode shown in Fig. 9(c). The spectrum consists of molecular ($E_l < 6$ eV) and atomic-like ($E_l \approx 9$ eV) contributions, very similar to the RIXS spectra of water⁸ and methanol.⁶ The other modes ν_4 , ν_7 , and ν_8 , excited in ACA, give additional contributions to the total RIXS profile, dressing it up with the secondary progression of 0.16 eV vibrational quanta corresponding to the ν_7 mode and a smaller contribution from the other modes. It is worth noting that the atomic-like peak of the ν_1 mode disappears in the multimode case. This can be explained by the fact that the core-excited wave packet is now trapped near the equilibrium by the multimode vibrational bath and thus cannot reach the dissociation region. This is in contrast to the case of the 1D ν_1 mode where the wave packet is released only on O–H bond elongation.

In the experimental RIXS spectrum, however, this long vibration progression is totally absent due to HB formation effects.¹² Indeed, as discussed in Sec. II A, the $O_H 1s \rightarrow \sigma^*$ state is shifted to the higher excitation energy range and is very much suppressed in intensity in the liquid phase due to the formation of the molecular chains, represented in our analysis by the molecular dimer. The HB-induced shift of the $O_H 1s \rightarrow \sigma^*$ state obviously removes fully the vibrational contribution related to this scattering channel, as illustrated in Fig. 10. The absence of the O–H vibrational progression as a result of the HB formation in the liquid phase allows us to make a quantitative analysis of the liquid ACA structure, which is still heavily debated in the literature.^{52,60,61} Based on the recent experiments using neutron scattering⁶² and Raman spectroscopy,⁶³ it is now commonly accepted that the liquid structure of ACA is similar to that of a disordered crystal with predominant chain structures. This conclusion is also confirmed by *ab initio* molecular dynamics

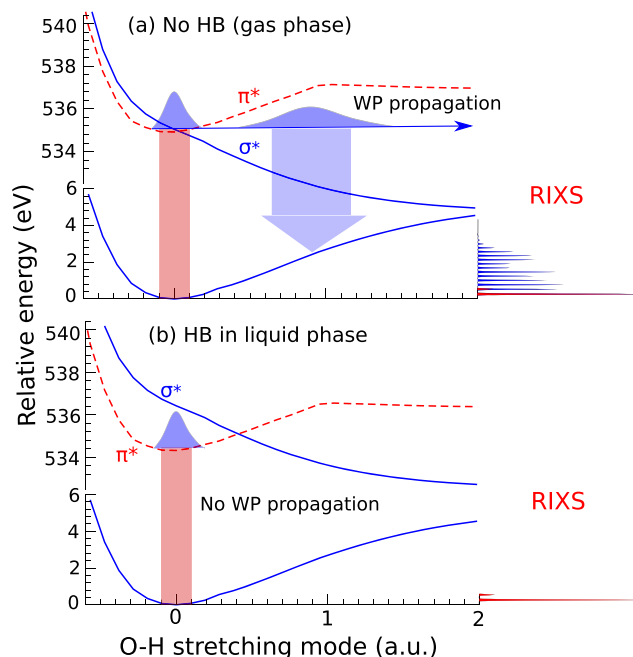


FIG. 10. Illustration of the vibrational progression formation in the quasi-elastic RIXS channel for the case (a) when no HB is formed and (b) for the HB present. One can clearly see the absence of the long vibrational progression in case (b).

simulations (see Ref. 12 and reference therein). However, the average length of the chain and admixture of the cycle structures broadly varies in different studies. The quenching of the vibrational progression in RIXS allows us to estimate the lower limit of ACA molecules in the average molecular chain. To do so, one can compare the number of OH groups not involved in HB formation (the groups at the ends of the molecular chain, “end” groups) with the number of OH groups forming HB (the groups “inside” the molecular chain). The RIXS from “end” groups should have O–H vibrational contributions, i.e., from the ν_1 mode, while RIXS from “inside” OH groups has no vibrational contributions from the O–H stretching mode. Given that the contribution from the “end” O–H groups should be small enough and that the ν_1 vibrational peaks are smaller or the same as the experimental noise level, the average number of units in molecular chains of liquid ACA can be estimated as ≥ 3.5 . The details of this analysis can be found elsewhere¹² and are thus omitted here.

Contrary to the $O_H 1s \rightarrow \sigma^*$ state, the $O_H 1s \rightarrow \pi^*$ core-excited state does not change much due to HB formation. As already discussed (Figs. 6 and 7), the XAS feature related to the $O_H 1s \rightarrow \pi^*$ excitation in the dimer experiences only a small red shift as compared to gas phase ACA. Moreover, the ν_1 mode is completely inactive in the RIXS via the $O_H 1s \rightarrow \pi^*$ state, since the PECs of the ground and core-excited states are nearly parallel (see the illustration in Fig. 10). This phenomenon can be understood from the fact that the π^* -state, located on the O–H bond, has its main contribution from the O $2p$ atomic orbitals and, obviously, no contribution from the hydrogen p -orbital. Due to this, the O–H bond elongation does not change the electronic structure of the excited state very much. On the other hand, excitation to the π^* located on C=O bond has strong contributions from both O $2p$ and C $2p$ orbitals, which affect very much the PEC along C=O elongation and give a strong vibrational progression in RIXS, as discussed in Sec. III D 1. As a result, our theoretical simulations of the quasi-elastic RIXS channel via an isolated $O_H 1s \rightarrow \pi^*$ state give rather good agreement with experimental spectra for the liquid phase, as shown in Fig. 9(b).

The main vibrational contribution in this case is given from the C–O stretching (ν_8) and C–O–H bending (ν_7) modes. The experimental resolution allows us to see clearly excitations in the vibrational progression of 0.16 eV (ν_7 mode). In our multimode theoretical analysis for the monomer, the progression related to the ν_8 (C–O stretching) mode gives the main contribution to the total RIXS spectrum (thick black line), while the ν_7 mode contributes to the formation of the right-hand side shoulder of the peaks. This difference can be explained by the independent-mode approximation we used here. Let us note that these two modes have close frequencies and show quite similar atomic coordinates displacement (Fig. 2, Table I). A more accurate two-dimensional wave packet propagation on a two-dimensional potential energy surface along these two vibrational modes could change the relative vibrational contribution profoundly, as it was observed in the case of water.⁷ These simulations, however, are rather time consuming for ACA and go beyond the scope of the present study. Another possible reason for the experimental–theoretical disagreement is slight modifications of the PECs in liquid phase as compared to the gas phase (see Fig. 4). Overall, the theoretical–experimental comparison gives a reasonable agreement in the length of the vibrational progression and vibrational contributions from different modes.

E. Vibrational structure of the inelastic scattering channels

The electronic assignment of the RIXS features was given in Sec. III C; here, we discuss changes in the RIXS profile due to the vibrational excitation in final electronic states different from the ground state. The multimode RIXS analysis for the ACA monomer is presented in Fig. 11. In order to compare our results to the experimental RIXS, we show only channels, which contribute in the liquid phase (when the HB with the O_H atom is formed), namely, the channels involving the $O_C 1s \rightarrow \pi^*$ [Fig. 11(a)] and $O_H 1s \rightarrow \pi^*$ [Fig. 11(b)] core-excited states leading to the $\sigma - \pi^*$ and $\pi - \pi^*$ final states. The contributions from these channels are indicated in red lines in the electronic RIXS analysis in Fig. 8.

One can clearly see that the spectral profile for the valence excited final states is formed from strong vibrational contributions from all considered vibrational modes, contrary to the quasi-elastic RIXS case, where the contribution from a single vibrational mode is usually dominating. This is a rather general phenomenon related to the large changes in the electronic structure due to valence electron excitations in the RIXS final states, leading to a substantial change in the molecular geometry (Fig. 3). However, the ν_1 mode is inactive in all inelastic scattering channels since no σ^* states are included. The first $\sigma \rightarrow \pi^*$ RIXS peak near 6 eV energy loss is dominating in the spectra at the $O_C 1s$ excitation and gives a rather weak contribution in the case of the O_H excitation. It is interesting to note that the

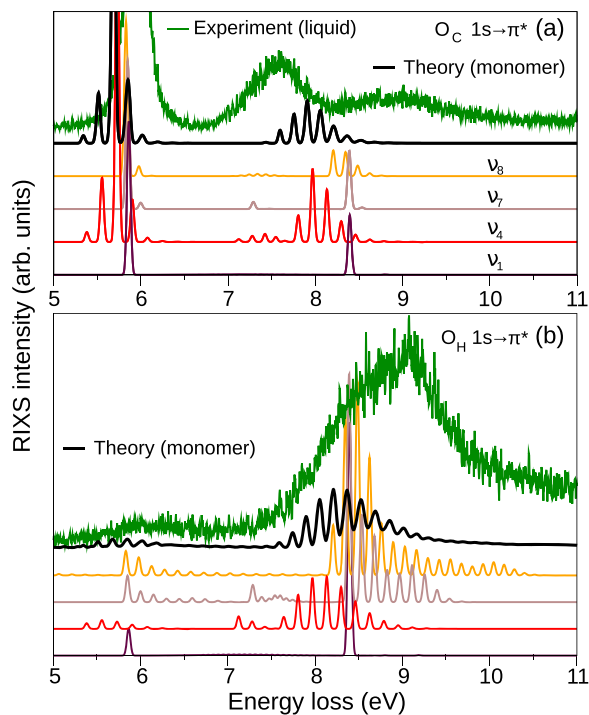


FIG. 11. Multimode theoretical RIXS from gas phase ACA (thick black line) via $O_C 1s \rightarrow \pi^*$ (a) and $O_H 1s \rightarrow \pi^*$ (b) core excited states. Individual contributions from the four main modes ν_1 , ν_4 , ν_7 , and ν_8 (see Table I) are shown. Experimental RIXS from liquid ACA (green line) is shown for comparison.

vibrational structure of the first RIXS peak involving the O_C excitation is similar to the vibrational structure observed in PES [Fig. 8(c)], as both are formed by the dominant contribution from the $13a'$ orbital.

The main contribution to the second structure in the RIXS spectrum is due to a $\pi \rightarrow \pi^*$ excitation and is found at 7.5 and 8.5 eV for O_C1s and O_H1s excitation, respectively. The energy of the valence excited state is overestimated in our theoretical calculations by about 0.5 eV, while the theoretical prediction of the PECs for the ACA monomer reasonably reproduced the vibrational broadening in comparison to the experimental spectra. The high energy part of the RIXS spectra above 8.5–9.0 eV is due to higher valence excited states not considered in the present study.

F. RIXS dependence on the excitation energy

Let us now discuss the RIXS dependence on the excitation energy detuning from the top of the XAS resonances $\Omega = \omega - \omega_{top}$. The detuning dependence analysis allows us to trace the vibrational dynamics by varying the effective scattering duration time $\tau = 1/\sqrt{\Gamma^2 + \Omega^2}$,⁵¹ which decreases with the increase in energy detuning. Due to this, the detuning works as a stop watch for the core-excited nuclear dynamics and along with isotope substitution study serves as a tool for the separation of the nuclear dynamics effect in the complex RIXS spectra from the effect related to the electronic excitation.^{5,6,8} Below, we focus on $O_C1s \rightarrow \pi^*$ and $O_H1s \rightarrow \pi^*$ core-excited states with XAS peak positions in the liquid phase at 532.1 and 534.6 eV, respectively. In each case, the detuning is defined with respect to the above mentioned peak maximum.

1. Quasi-elastic RIXS channels

The effect of the shortening of the vibrational progression for large detuning $|\Omega|$ from the resonance is clearly observed for the $O_C1s \rightarrow \pi^*$ excitation in both theory and experiment (see Fig. 12).

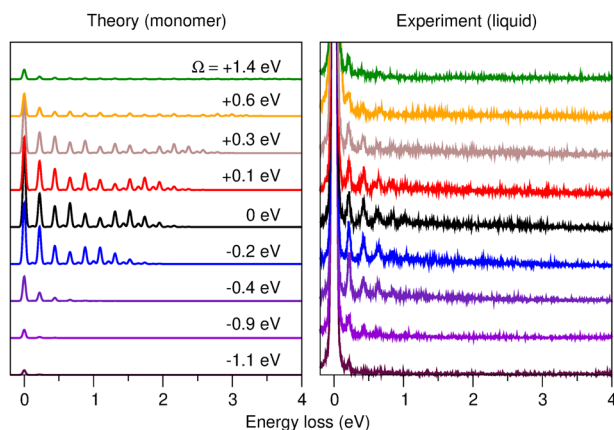


FIG. 12. Theoretical (monomer, left) and experimental (liquid, right) RIXS on the quasi-elastic channel via $O_C1s \rightarrow \pi^*$ resonance: dependence on the excitation energy. The excitation photon energy detuning from the top of the resonance $[\omega_{top}(O_C, \text{liquid}) = 532.1 \text{ eV}]$ is shown in the plot. Four vibrational modes (ν_1 , ν_4 , ν_7 , and ν_8) are taken into account.

However, this behavior is not symmetric for positive and negative detunings: due to a higher density of vibrational states above the resonance, the shortening of the vibrational progression is more pronounced when tuned below the resonance. In the theoretical results, the longest vibrational progression in RIXS is obtained near $\Omega = +0.3 \text{ eV}$, where resonance with an excited vibrational state is reached. This high core-excited vibrational wave function has a broader distribution along the PEC, resulting in the excitation of a longer vibrational progression in the RIXS spectrum. For the higher excitation energies, the RIXS intensity drops and mainly only the first (elastic) vibrational peak survives. Similar behavior in the detuning dependence is also found in the quasi-elastic RIXS channel via the $O_H1s \rightarrow \pi^*$ core-excited state, as shown in Fig. 13, while the formation of the vibrational profile was discussed above (see Fig. 9). Here, we excluded the $O_H1s \rightarrow \sigma^*$ channel from theory for comparison with the liquid phase experiment. Note that the peak near 0.66 eV energy loss, observed in the experimental spectra, is a spectrometer artifact and can be neglected. In both cases (i.e., $O_H1s \rightarrow \pi^*$ and $O_H1s \rightarrow \sigma^*$), all four main vibrational contributions are taken into account (ν_1 , ν_4 , ν_7 , and ν_8).

2. Inelastic RIXS channels

Let us now discuss the detuning dependence of the decay channels to the few lowest valence excited states, presented in the 5.0–9.0 eV energy loss region of RIXS (Fig. 8). The experimental RIXS spectral changes drastically when tuning the excitation energy from the O_C and O_H core-excited resonances. There are two main reasons for this: (i) different electronic transition dipole moments for the decay channels to the valence-excited states (see Sec. III C) and (ii) different vibrational excitations, which define the shape of the spectral line and its detuning dependence. Theoretical and experimental RIXS profiles for the $O_C \rightarrow \pi^*$ excitation in the range of 5.0–11.0 eV are summarized in Fig. 14 for different values of the detuning. Theoretical simulations reproduce the vibrational broadening of the two RIXS features as well as their energy shift with the detuning. Let us consider the vibrational profile of the corresponding core-excited state shown in Fig. 7 at 532 eV. One can see that, in the studied range of $\Omega = -1.1 \dots +1.4 \text{ eV}$, the photon energy nearly always comes into resonance with some vibrational level in

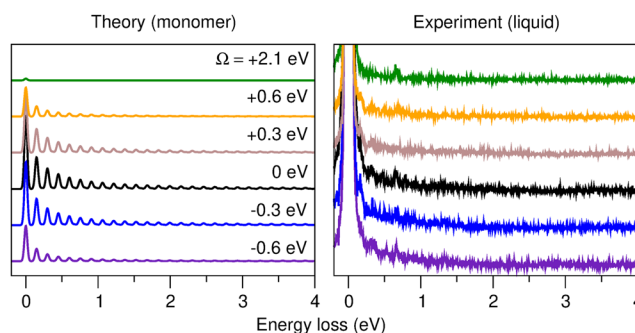


FIG. 13. Theoretical (monomer, left) and experimental (liquid, right) RIXS on the quasi-elastic channel via $O_H1s \rightarrow \pi^*$ resonance: dependence on the excitation energy. The excitation photon energy detuning from the top of the resonance $[\omega_{top}(O_H, \text{liquid}) = 534.6 \text{ eV}]$ is shown in the plot. Four vibrational modes (ν_1 , ν_4 , ν_7 , and ν_8) are taken into account.

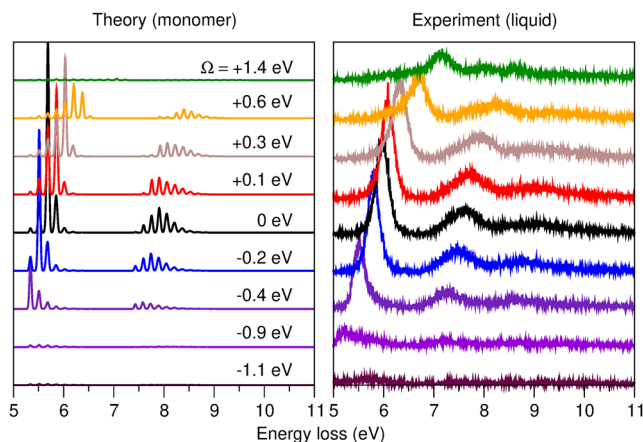


FIG. 14. Theoretical (monomer, left) and experimental (liquid, right) RIXS on the inelastic channel via O_C resonance: dependence on the excitation energy. The excitation photon energy detuning from the top of the resonance [$\omega_{top}(O_C, \text{liquid}) = 532.1$ eV] is shown in the plot. Four vibrational modes (ν_1 , ν_4 , ν_7 , and ν_8) are taken into account.

the core-excited state. Due to this, the RIXS vibrational profile alters drastically with changes in the excitation energy. This observation relates also to the change of the spectra center of gravity, so the spectral features are preserved at the same emission energy (no Raman dispersion), which is confirmed by the experiment.

The situation changes drastically when the excitation energy is tuned to the second core-excited resonance $O_H \rightarrow \pi^*$ (Fig. 15). One can see an energy shift of the spectral feature near $E_f \approx 8$ eV in the experiment, while in theory, the center of gravity of the feature is preserved at nearly the same position. This discrepancy can be explained by the contribution from another higher valence-excited state not considered in our theoretical model. Indeed, one can see the formation of an additional peak (peak splitting) at 9.5 eV for $\Omega = 0.6$ eV. Another possible explanation is related to a change in the PECs of the ACA dimer as compared to the monomer used in the present simulations.

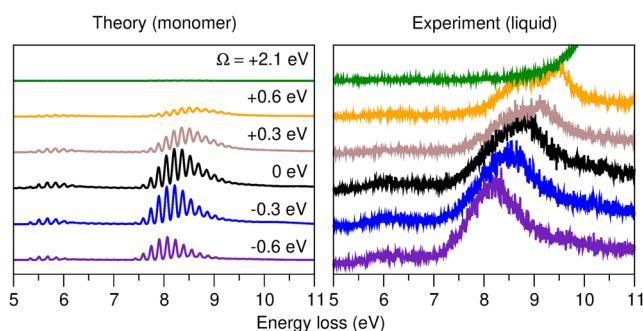


FIG. 15. Theoretical (monomer, left) and experimental (liquid, right) RIXS on the inelastic channel via O_H resonance: dependence on the excitation energy. The excitation photon energy detuning from the top of the resonance [$\omega_{top}(O_H, \text{liquid}) = 534.6$ eV] is shown in the plot. Four vibrational modes (ν_1 , ν_4 , ν_7 , and ν_8) are taken into account.

IV. CONCLUSIONS

We have performed a detailed study of the RIXS from acetic acid via the two lowest spectral features at the oxygen K-edge, related to the $O_C 1s$ and $O_H 1s$ electronic excitations. Theoretical simulations for the isolated molecule and for the dimers are compared to the experimental measurements performed in liquid phase. Using the dimer model, we were able to identify and explain the formation of the main spectral features in the liquid phase experiment. The theoretical description combines high level *ab initio* [RASPT2 and ADC(2)-x] and DFT calculations of the electronic structure and transitions in the isolated molecule and two types of dimers (symmetric dimer and inverted dimer). These approaches are complementary to each other and show good agreement. The vibrational dynamics was taken into account at a quantum mechanical level by a hybrid time-dependent and stationary approach for the solution of the nuclear Schrödinger equation. Within this approach, the dissociative or quasi-dissociative dynamics can be treated in the time-dependent framework, while the other vibrational modes are included in the Franck–Condon approximation. Such an advanced theoretical treatment allowed us to compute relatively cheaply the multi-mode vibrational excitation (four vibrational modes). The combination of the advanced theory and high-resolution experiment, presented in this paper, makes it possible to draw important conclusions from the comparison of the molecules in the gas and liquid phases.

The character of the core-excited state changes drastically when the hydrogen bond is formed in the liquid phase, which can be fully resolved in the RIXS spectrum. Strict theoretical modeling of the formation of the vibrationally resolved RIXS for the liquid phase is very complex. We show, however, that this analysis can be done qualitatively, yet in a good agreement with experiment, with the help of a detailed understanding of the RIXS spectra for the isolated molecule. The potential energy curves computed for the ACA dimer provide us with a robust model for the nuclear dynamics in the liquid phase. The energy detuning from the top of resonance shows clearly the suppression of the effect related to the nuclear dynamics and explains the details of the dynamics in the final (valence-excited) states of RIXS. The present study of ACA shows an example of how a combined theoretical–experimental RIXS analysis can be used for the accurate study of quantum nuclear dynamics of liquids. We believe that the methods presented here will find further applications for more complex systems.

ACKNOWLEDGMENTS

This work was supported by the Swedish Research Council (Grant Nos. 2019-03470, 2018-4343, and 2017-06419) and the Russian Science Foundation (Project No. 16-12-10109). M.O. acknowledges financial support from the Carl Tryggers Foundation (Grant CTS18:285) and the European Union’s Horizon 2020 research and innovation programme under the Marie Skłodowska-Curie Grant Agreement No. 860553. F.G. acknowledges the support from the Helmholtz Virtual Institute VI419 “Dynamic Pathways in Multidimensional Landscapes.” The research work of V.S. was partially funded by a Swedish Institute scholarship. The synchrotron experiments were performed at the ADDRESS beamline of the Swiss Light Source at the Paul Scherrer Institut (PSI). The work

at PSI was supported by the Swiss National Science Foundation through the NCCR MARVEL and the Sinergia project “Mott Physics Beyond the Heisenberg (MPBH) model” (SNSF Research Grant Nos. CRSII2:141962 and CRSII2:1607651). The research leading to these results received funding from the European Community’s Seventh Framework Programme (No. FP7/2007–2013) under Grant Agreement No. 290605 (COFUND: PSIFELLOW). The calculations were enabled by resources provided by the Swedish National Infrastructure for Computing (SNIC) partially funded by the Swedish Research Council through Grant Agreement No. 2018-05973.

APPENDIX: AVERAGING OVER MOLECULAR ORIENTATION

In order to account for the isotropic molecular orientation distribution in the gas phase, we perform orientation averaging.⁵ The dependence of the RIXS cross section (2) on molecular orientation comes from the relative orientation of the transitions dipole moments on the ground to core-excited and core-excited to final states transitions, \mathbf{d}_{eg} and \mathbf{d}_{fc} , respectively, which are considered independent of the geometry in the present study. In order to compute RIXS cross sections, we have to average over molecular orientations of the following product of the transition dipole moments:

$$\begin{aligned}\zeta_{cf}(\theta) &= \overline{(\mathbf{e} \cdot \mathbf{d}_{eg})(\mathbf{e} \cdot \mathbf{d}_{eg})(\mathbf{e}' \cdot \mathbf{d}_{fc})(\mathbf{e}' \cdot \mathbf{d}_{fc})} \\ &= \frac{d_{eg}^2 d_{fc}^2}{15} [2 - \cos^2 \theta + (3 \cos^2 \theta - 1)(\hat{\mathbf{d}}_{fc} \cdot \hat{\mathbf{d}}_{eg})^2], \quad (\text{A1})\end{aligned}$$

where $\theta = \angle(\mathbf{e}', \mathbf{e})$ is the angle between polarization vectors of the incoming \mathbf{e} and outgoing \mathbf{e}' photons and $\hat{\mathbf{d}}_{fc}$ and $\hat{\mathbf{d}}_{eg}$ are unit vectors showing the direction of the corresponding transition dipole moments in the chosen molecular frame (see Fig. 2). The components of the transition dipole moments for all RIXS channels of interest are collected in Table III. Equation (A1) can be written in a standard way using the anisotropy parameter β_θ ,

$$\begin{aligned}\zeta_{cf}(\theta) &= \frac{d_{eg}^2 d_{fc}^2}{9} [1 + \beta_\theta (3 \cos^2 \theta - 1)], \\ \beta_\theta &= \frac{\zeta_{cf}(0^\circ) - \zeta_{cf}(90^\circ)}{\zeta_{cf}(0^\circ) + 2\zeta_{cf}(90^\circ)} = \frac{1}{5} [3(\hat{\mathbf{d}}_{fc} \cdot \hat{\mathbf{d}}_{eg})^2 - 1].\end{aligned} \quad (\text{A2})$$

Conventional soft x-ray spectrometers, however, collect scattered x-ray photons with all polarizations. In this case, one should average the RIXS cross section over the orientations of the outgoing polarization vector \mathbf{e}' around the momentum vector of the emitted x-ray photon $\hat{\mathbf{k}}'$. This results in the following replacement in the above equations:

$$\begin{aligned}\overline{\cos^2 \theta} &= \frac{1}{2} \sin^2 \chi = \frac{1}{2} [1 - (\mathbf{e} \cdot \hat{\mathbf{k}}')^2], \\ \chi &= \angle(\mathbf{e}, \hat{\mathbf{k}}').\end{aligned} \quad (\text{A3})$$

Then, the average coefficient for the RIXS cross sections reads

$$\begin{aligned}\zeta_{cf}(\chi) &= \frac{d_{eg}^2 d_{fc}^2}{9} [1 + \beta_\chi (3 \cos^2 \chi - 1)], \\ \beta_\chi &= \frac{\zeta_{cf}(0^\circ) - \zeta_{cf}(90^\circ)}{\zeta_{cf}(0^\circ) + 2\zeta_{cf}(90^\circ)} = \beta_\theta / 2.\end{aligned} \quad (\text{A4})$$

This equation is used in our simulations and comparisons with experiment, which is performed at $\chi = 90^\circ$. The computed coefficients $\zeta_{cf}(90^\circ)$ are collected in Table III.

DATA AVAILABILITY

The data that support the findings of this study are available from the corresponding author upon reasonable request.

REFERENCES

- P. Wernet *et al.*, *Science* **304**, 995 (2004).
- T. Tokushima *et al.*, *Phys. Chem. Chem. Phys.* **11**, 1679 (2009).
- A. Pietzsch *et al.*, *Phys. Rev. Lett.* **114**, 088302 (2015).
- V. Vaz da Cruz *et al.*, *Nat. Commun.* **10**, 1013 (2019).
- E. Ertan *et al.*, *Phys. Chem. Chem. Phys.* **20**, 14384 (2018).
- V. Vaz da Cruz *et al.*, *J. Chem. Phys.* **150**, 234301 (2019).
- R. C. Couto *et al.*, *Nat. Commun.* **8**, 12725 (2017).
- V. Vaz da Cruz *et al.*, *Phys. Chem. Chem. Phys.* **19**, 19573 (2017).
- M. Odelius, *Phys. Rev. B* **79**, 144204 (2009).
- Y. Harada *et al.*, *Phys. Rev. Lett.* **111**, 193001 (2013).
- J. Niskanen *et al.*, *Proc. Natl. Acad. Sci. U. S. A.* **116**, 4058 (2019).
- V. Savchenko *et al.*, *Sci. Rep.* **11**, 4098 (2021).
- V. N. Strocov *et al.*, *J. Synchrotron Radiat.* **17**, 631 (2010).
- G. Ghiringhelli *et al.*, *Rev. Sci. Instrum.* **77**, 113108 (2006).
- F. Hennies *et al.*, *Phys. Rev. Lett.* **104**, 193002 (2010).
- M. B. Robin, I. Ishii, R. McLaren, and A. P. Hitchcock, *J. Electron Spectrosc. Relat. Phenom.* **47**, 53 (1988).
- U. Mölder, I. Koppel, P. Burk, and R. Pikver, *Int. J. Quantum Chem.* **62**, 303 (1997).
- F. Aquilante *et al.*, *J. Comput. Chem.* **37**, 506 (2016).
- P.-O. Widmark, P. k. Malmqvist, and B. r. O. Roos, *Theor. Chim. Acta* **77**, 291 (1990).
- M. Douglas and N. M. Kroll, *Ann. Phys.* **82**, 89 (1974).
- B. A. Hess, *Phys. Rev. A* **33**, 3742 (1986).
- P.-Å. Malmqvist and B. O. Roos, *Chem. Phys. Lett.* **155**, 189 (1989).
- P. Å. Malmqvist, B. O. Roos, and B. Schimmelpfennig, *Chem. Phys. Lett.* **357**, 230 (2002).
- I. Fdez. Galván *et al.*, *J. Chem. Theory Comput.* **15**, 5925 (2019).
- M. Guo, L. K. Sørensen, M. G. Delcey, R. V. Pinjari, and M. Lundberg, *Phys. Chem. Chem. Phys.* **18**, 3250 (2016).
- A. D. Becke, *Phys. Rev. A* **38**, 3098 (1988).
- J. P. Perdew, *Phys. Rev. B* **34**, 7406 (1986).
- N. Godbout, D. R. Salahub, J. Andzelm, and E. Wimmer, *Can. J. Chem.* **70**, 560 (1992).
- W. Kutzelnigg, U. Fleischer, and M. Schindler, *NMR-Basic Principles and Progress* (Springer-Verlag, Heidelberg, 1990).
- L. G. M. Pettersson, U. Wahlgren, and O. Gropen, *J. Chem. Phys.* **86**, 2176 (1987).
- M. J. Frisch *et al.*, Gaussian 16, Revision B.01, Gaussian, Inc., Wallingford, CT, 2016.
- C. Möller and M. S. Plesset, *Phys. Rev.* **46**, 618 (1934).
- M. J. Frisch, M. Head-Gordon, and J. A. Pople, *Chem. Phys. Lett.* **166**, 275 (1990).
- M. J. Frisch, M. Head-Gordon, and J. A. Pople, *Chem. Phys. Lett.* **166**, 281 (1990).
- M. Head-Gordon, J. A. Pople, and M. J. Frisch, *Chem. Phys. Lett.* **153**, 503 (1988).
- S. Sæbø and J. Almlöf, *Chem. Phys. Lett.* **154**, 83 (1989).
- M. Head-Gordon and T. Head-Gordon, *Chem. Phys. Lett.* **220**, 122 (1994).
- T. H. Dunning, Jr., *J. Chem. Phys.* **90**, 1007 (1989).
- R. A. Kendall, T. H. Dunning, Jr., and R. J. Harrison, *J. Chem. Phys.* **96**, 6796 (1992).

- ⁴⁰K. A. Peterson, D. E. Woon, and T. H. Dunning, Jr., *J. Chem. Phys.* **100**, 7410 (1994).
- ⁴¹S. F. Boys and F. Bernardi, *Mol. Phys.* **19**, 553 (1970).
- ⁴²S. Simon, M. Duran, and J. J. Dannenberg, *J. Chem. Phys.* **105**, 11024 (1996).
- ⁴³M. Wormit *et al.*, *Mol. Phys.* **112**, 774 (2014).
- ⁴⁴Y. Shao *et al.*, *Mol. Phys.* **113**, 184 (2015).
- ⁴⁵J. Wenzel, M. Wormit, and A. Dreuw, *J. Comput. Chem.* **35**, 1900 (2014).
- ⁴⁶J. Wenzel, A. Holzer, M. Wormit, and A. Dreuw, *J. Chem. Phys.* **142**, 214104 (2015).
- ⁴⁷J. Wenzel and A. Dreuw, *J. Chem. Theory Comput.* **12**, 1314 (2016).
- ⁴⁸R. Krishnan, J. S. Binkley, R. Seeger, and J. A. Pople, *J. Chem. Phys.* **72**, 650 (1980).
- ⁴⁹T. Clark, J. Chandrasekhar, G. W. Spitznagel, and P. V. R. Schleyer, *J. Comput. Chem.* **4**, 294 (1983).
- ⁵⁰A. Bergner, M. Dolg, W. Küchle, H. Stoll, and H. Preuß, *Mol. Phys.* **80**, 1431 (1993).
- ⁵¹F. Gel'mukhanov and H. Ågren, *Phys. Rep.* **312**, 87 (1999).
- ⁵²O. Takahashi, N. Nishida, S. Kanai, Y. Horikawa, and T. Tokushima, *J. Phys.: Conf. Ser.* **712**, 012040 (2016).
- ⁵³T. Shimanouchi, H. Matsuura, Y. Ogawa, and I. Harada, *J. Phys. Chem. Ref. Data* **7**, 1323 (1978).
- ⁵⁴F. Carnovale, T. H. Gan, and J. B. Peel, *J. Electron Spectrosc. Relat. Phenom.* **20**, 53 (1980).
- ⁵⁵P. Limão-Vieira *et al.*, *Chem. Phys.* **324**, 339 (2006).
- ⁵⁶S. Eckert *et al.*, *Phys. Rev. A* **97**, 053410 (2018).
- ⁵⁷Y.-P. Sun *et al.*, *Phys. Rev. B* **84**, 132202 (2011).
- ⁵⁸C. M. Johnson, E. Tyrode, S. Baldelli, M. W. Rutland, and C. Leygraf, *J. Phys. Chem. B* **109**, 321 (2005).
- ⁵⁹J. Semmler and D. E. Irish, *J. Solution Chem.* **17**, 805 (1988).
- ⁶⁰S. Riniker *et al.*, *ChemPhysChem* **13**, 1182 (2012).
- ⁶¹M. Zhang, L. Chen, H. Yang, and J. Ma, *J. Phys. Chem. A* **121**, 4560 (2017).
- ⁶²A. Chebaane, S. Trabelsi, S. Nasr, and M.-C. Bellissent-Funel, *J. Mol. Liq.* **198**, 204 (2014).
- ⁶³T. Nakabayashi, K. Kosugi, and N. Nishi, *J. Phys. Chem. A* **103**, 8595 (1999).
- ⁶⁴S. R. Smith and T. D. Thomas, *J. Am. Chem. Soc.* **100**, 5459 (1978).